Eur Biophys J (2005) 34: 181–199
DOI 10.1007/s00249-004-0441-0

ARTICLE

Arne Gennerich · Detlev Schild

Sizing-up finite fluorescent particles with nanometer-scale precision by convolution and correlation image analysis

Received: 17 June 2004 / Revised: 6 September 2004 / Accepted: 21 September 2004 / Published online: 18 December 2004

Abstract Determining the positions, shapes and sizes of finite living particles such as bacteria, mitochondria or vesicles is of interest in many biological processes. In fluorescence microscopy, algorithms that can simultaneously localize such particles as a function of time and determine the parameters of their shapes and sizes at the nanometer scale are not yet available. Here we develop two such algorithms based on convolution and correlation image analysis that take into account the position, orientation, shape and size of the object being tracked, and we compare the precision of the two algorithms using computer simulations. We show that the precision of both algorithms strongly depends on the object's size. In cases where the diameter of the object is larger than about four to five times the beam waist radius, the convolution algorithm gives a better precision than the correlation algorithm (it leads to more precise parameters), while for smaller object diameters, the correlation algorithm gives superior precision. We apply the convolution algorithm to sequences of confocal laser scanning micrographs of immobile *Escherichia coli* bacteria, and show that the centroid, the front end, the rear end, the left border and the right border of a bacterium can be determined with a signal-to-noise-dependent precision down to ~5 nm.

Keywords Correlation · Convolution · Tracking precision · Accuracy · *Eschericha coli* · Laser Scanning Microscopy

Introduction

Single-particle tracking (SPT) is a tool that is often used in biophysical research to observe displacements and trajectories of small fluorescent particles in motility assays and in cell membranes (Saxton and Jacobson 1997). Depending on the object and background intensity in subsequent images, a localization and tracking precision down to the nanometer scale can be achieved (Yildiz et al. 2003). Common SPT algorithms give reliable results if the object being tracked has a constant diameter that is markedly smaller than the wavelength of the fluorescent light. However, these standard algorithms fail in cases where a finite particle with a diameter similar to the wavelength of light changes shape, size or orientation during tracking. Here we report on the computer analysis of images taken from fluorescence-labeled *Escherichia coli* bacteria in vitro. We derive equations for convolution and auto- and cross-correlation image analysis that take into account shape, size, orientation and position of the object being tracked, and quantitatively compare the accuracy and the precision of both algorithms by computer simulations. Measurements were performed using a home-built instrument that combines the advantages of fluorescence correlation spectroscopy (FCS) (Krichevsky and Bonnet 2002; Kim and Schwille 2003) and confocal laser scanning microscopy (CLSM). Analyzing subsequent CLSM images of immobile fluorescent bacteria with the finite particle tracking (FPT) algorithms developed demonstrate that the edges and the centroid of sausage-like structures, like bacteria, can be determined with a precision down to 5 nm. The models for FPT analysis introduced here open up the possibility of high-precision localization and tracking of vesicles and various types of regularly-shaped organelles both in vitro and in vivo.

Materials and methods

E. coli bacteria

E. coli bacteria of the substrain K12 were obtained from standard laboratory cloning experiments. Prior to imaging, the bacteria were diluted and applied in a drop of

A. Gennerich · D. Schild (✉)
Physiologisches Institut, Universität Göttingen,
Humboldtallee 23 D 37073, Göttingen, Germany
E-mail: dschild@gwdg.de
Tel.: +49-551-395915
Fax: +49-551-398399

solution onto a coverslip placed on the microscope stage. The composition of the bath solution was (in mM): NaCl 98, KCl 2, $MgCl_2$ 2, $CaCl_2$ 1, Glucose 5, PyruvatNa 5, HEPES 10, 225 mOsm, pH 7.8. Under these conditions the bacteria were immobile. *E. coli* bacteria were labeled with the fluorescent dye MitoTracker Orange CMTROs (Molecular Probes, Leiden, The Netherlands), a lipophilic cationic dye derived from Tetramethylrosamin for staining living mitochondria. Prior to the CLSM measurements, *E. coli* bacteria were incubated for ~10 min in 100 nM MitoTracker dissolved in the bath solution. MitoTracker accumulated preferentially in *E. coli* due to the negative transmembrane potential of the bacteria. Measurements were performed after rinsing of the bath. An inverted Zeiss Axiovert 35 microscope (Carl Zeiss, Göttingen, Germany) was used to which the following apparatus was attached.

Combined CLSM and FCS set-up

Figure 1 shows the imaging set-up used (previously described in detail, Gennerich and Schild, 2000). Briefly, a HeNe cw-laser (2.2 mW) at 543.5 nm was used as the excitation source (LK 54015, Laser Graphics, Dieburg, Germany). Tandem galvanometer mirrors (GD120DT, GSI Lumonics, Unterschleissheim, Germany) were used for x-y-positioning, and a piezo-driven objective holder (P-721.10, Physik Instrumente, Waldbronn, Germany) for z-positioning. The back aperture of the objective used (C-Apochromat 40/1.2 W, Carl Zeiss) was not overilluminated. The laser intensity was set to 3.14 kW/cm^2 using neutral density filters. The detection pinhole had a diameter of 50 µm. The beam waist radius and the structure factor were determined to be $r_{xy} = 0.24$ µm and $S = r_z/r_{xy} = 7$ by FCS measurements of translational three-dimensional diffusion of tetramethylrhodamine (TMR) (T-5646, Sigma-Aldrich Chemie, Deisenhofen, Germany) in water, assuming a diffusion constant of $D = 2.8 \times 10^{-6} cm^2/s$ (Rigler et al. 1993).

Two personal computers were used to control the experiment and data acquisition; for simplicity these are termed LSM-PC and FCS-PC here. Pulses generated by the single photon-counting module (SPCM-AQ-141, EG&G, Optoelectronics, Dumberry, Canada) were transformed into TTL pulses with the same pulse width and sent to both PCs. The FCS-PC was equipped with a hardware correlator board (ALV-5000/E, ALV, Langen, Germany). The LSM-PC had two additional hardware cards: first, a DSP-card (ADwin-9, Jäger Messtechnik GmbH, Lorch, Germany) with 12-bit ADCs and DACs, and second, a PCI controller interface (PCI-Proto LAB, H + K Messsysteme GmbH, Berlin, Germany). CLSM measurements were controlled using a custom-developed graphics interface (image processing software, IPS) running under the RT-Linux operating system. The DSP-card generated the control voltages and sent them to the x- and y-galvanometer control hardware, and sampled (12 bit, 10 µs) the x-position signal. The x-y-position of the confocal detection volume was calculated based on the known relationship between low frequency control voltage changes and the corresponding changes in the spatial coordinates in the object plane, the known periodicity of the control voltages, and the measured phase shift between the sampled horizontal position signal and the corresponding galvanometer input signal. Images were only calculated for the quasi-linear range of

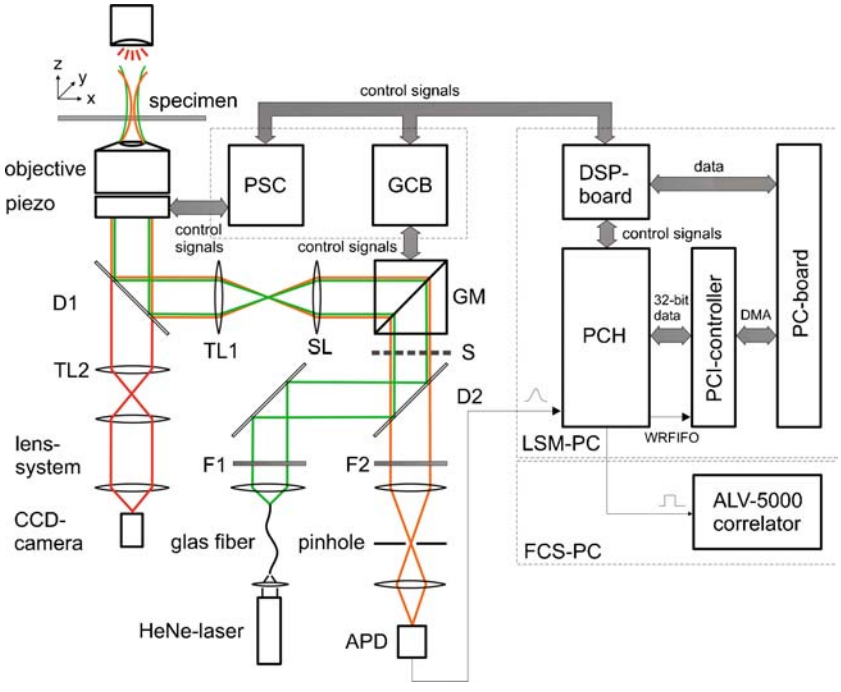

Fig. 1 Schematic of the combined CLSM and FCS set-up. For a detailed description, see text. Components: F1: neutral density filter; F2: interference filter; D1: dichroic mirror (BSP690, DELTA Light & Optics, Lyngby, Denmark); D2: dichroic mirror (BSP-25-560, DELTA Light & Optics); GM: tandem galvanometer mirrors; GCB: galvanometer controller boards (AE1000 Controller Boards, GSI Lumonics); PSC: piezo servo controller (E-610.L0, Physik Instrumente, Waldbronn, Germany); PCH: photon counting hardware; SL: scan lens; TL1/2: tube lens

galvanometer positions (the range within which the focus volume has a constant pixel dwell time). Communication between the DSP-card and PC was interrupt-controlled by PC-DSP communication software supplied by the vendor (Jäger Messtechnik GmbH, Lorch, Germany). During CLSM measurements, the photons captured by the APD were transformed into TTL pulses and sent to the PCI-card. Custom-made electronics put the pulses into a 32-bit shift register, and transferred them via DMA to the LSM-PC's RAM. CLSM images were formed by assigning the photon counts at a given time interval (dwell time) to the pixel resulting for that time interval from the calculated position of the detection volume. The images were displayed as image sequences on the monitor.

The detection efficiency of the avalanche photodiode used was 70-80%. Backreflection ($\lambda_{exc} = 543.5$ nm) was blocked by an interference filter (HQ 582/50, OD6, AF Analysetechnik, Pfrondorf, Germany) placed in front of the photodiode. Using an APD allows virtually noise-free measurements. The APD used had a dark count rate of 100/s. Given a typical pixel dwell time of 4 µs, this means that there is one spurious photon every 2500 pixels. On the other hand, the deadtime of the APD limits the bandwidth. The inset of Fig. 2a shows the mean count rate $\langle N \rangle$ of the APD as a function of the deadtime-corrected mean count rate $\langle N' \rangle$ (data supplied by EG&G, Optoelectronics, Dumberry, Canada). The deadtime of the detector leads to an underestimation of the number of incident photons if the number exceeds ~1 Mcps (cps, counts per second), and the photon count variance σ over the number of photons detected (Fig. 2b) deviates from the linearity typical of Poisson processes (Yu and Fessler 2000). Furthermore, the deadtime leads to an increased relative standard deviation r of the photodetector countrate N at rates below $\sim 15 \times 10^6 s^{-1}$ (Fig. 2a) as compared to the relative standard deviation r' of the Poisson-distributed countrate N' of a photodetector without deadtime (Fig. 2a). This effect results in a reduced SNR for the images. As the localization precision (σ) of the object coordinates

Fig. 2a–d Photon-counting with deadtime. **a** Relative standard deviation $r = \sqrt{\langle \delta N^2 \rangle} / \langle N \rangle$ of the photon count rate N as a function of the mean count rate $\langle N \rangle$, measured using the photon detection system of our set-up (*solid line*). The calculation of r is based on the variance $\langle \delta N^2 \rangle$ as a function of $\langle N \rangle$ as given by the fitted fourth-order polynominal shown in plot (b) of this figure. The dashed line shows the relative standard deviation $r' = \sqrt{\langle \delta N'^2 \rangle} / \langle N' \rangle = \sqrt{\langle N' \rangle} / \langle N' \rangle = 1 / \sqrt{\langle N' \rangle}$ of the Poisson-distributed count rate N' as a function of the deadtime-affected mean count rate $\langle N \rangle$ with $\langle N' \rangle$ being the deadtime-corrected mean count rate. The conversion from $\langle N' \rangle$ to $\langle N \rangle$ follows from the fitted theoretical function shown in the inset. The inset of this figure depicts the mean count rate $\langle N \rangle$ as a function of the deadtime-corrected mean count rate $\langle N' \rangle$ (*closed circles*, data supplied by EG&G, Optoelectronics, Dumberry, Canada). The *solid line* shows the fitted theoretical function $\langle N \rangle = \langle N' \rangle t / (1 + \langle N' \rangle \tau)$ for a non-paralyzable detection system (Yu and Fessler 2000). Result of the fit: $t = 0.647$ µs and $\tau = 31$ ns ($\langle N' \rangle$ in $10^6 s^{-1}$). τ is the mean detector deadtime. **b** Variance $\langle \delta N^2 \rangle$ of the count rate N as a function of the mean count rate $\langle N \rangle$, measured with the photon detection system used herein (*closed circles*). The data points come from measurements performed in a drop of 1 mM TMR solution placed onto a coverslip. The mean intensity of each successive measurement was increased step by step by moving the confocal detection volume into the drop of TMR solution using the piezo-driven objective holder, beginning at a position within the 160 µm-thick coverslip (below the drop of TMR solution ($I_a = 374$ kW/cm^2)). Fitting a fourth-order polynomial gave ($\langle N \rangle$ in $10^6 s^{-1}$): $\langle \delta N^2 \rangle = 1.04892 \langle N \rangle - 0.05101 \langle N \rangle^2 - 0.00158 \langle N \rangle^3 + 0.00008 \langle N \rangle^4$ (*solid line*). The *dashed line* shows the theoretical variance of a Poisson-distributed count rate with $\langle \delta N^2 \rangle = \langle N \rangle$. **c** Example taken from one of the successive measurements, a 1 ms portion of a measurement of 220 ms duration is shown ($\langle N \rangle = 8.41 \times 10^6 s^{-1}$). **d** Histogram of the measured count-rates (part of the corresponding measurement is shown in plot (c) of this figure). Fitting a Gaussian function results in $\langle N \rangle = 29.03$ and $\sigma = 3.99$ (*solid line*)

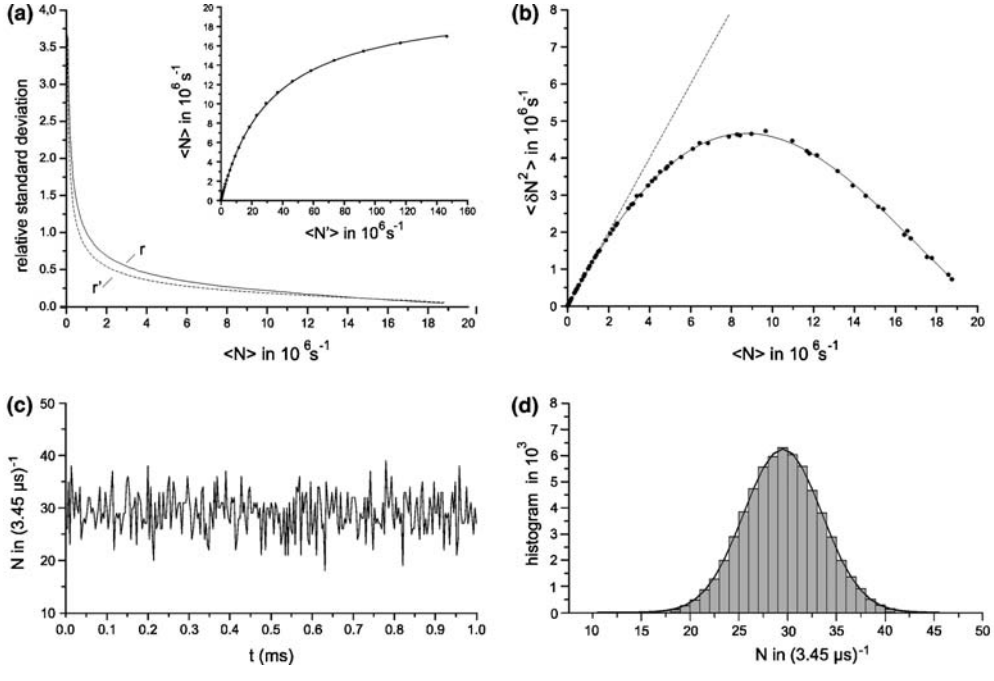

strongly depends on the SNR of the images, the precision discussed in this paper indicates the upper limit of achievable precision. In addition, the measured photon countrate (Fig. 2c) is well described by a Gaussian distribution (Fig. 2d) in contrast to photon signals of other photodetectors (such as photomultipliers) that exhibit Poisson-statistics.

Image analysis and computer simulations

Analysis of experimental CLSM images and computer simulations were performed under the Linux operating system using the IDL computer language (Research Systems, Boulder, CO, USA). Normalized autocorrelation- and cross-correlation functions of subsequent images were calculated using IDL subroutines. Software routines for numerical integration and image-fitting procedures based on the Levenberg-Marquarth algorithm (Marquarth 1963), were obtained from sources in the public domain. Simulated fluorescence images of *E.coli* bacteria were calculated by adding shot noise to the theoretical noise-free intensity distribution $I(x_i,y_i)$ describing the model object (see below). For a pixel with coordinates (x_i,y_i), a random intensity value was generated from a Poisson distribution with mean intensity $I(x_i,y_i)$ at that pixel.

Signal-to-noise ratio (SNR)

The localization precision of the algorithms derived here strongly depends on the size of the object, its intensity, the background signal, the resolution of the imaging system and the pixel size (Bobroff 1986; Cheezum et al. 2001; Thompson et al. 2002). The precision of an algorithm, defined by the standard deviation of a fitted parameter (Kues et al. 2001), is a measure of the range within which a parameter can fall. Because a measurement can be precise without being accurate, both the localization precision and accuracy of an algorithm must be taken into account. Here, the accuracy of the algorithm is defined as the deviation between the true parameter and the mean of the parameter subsequently estimated (for a detailed investigation of the accuracy and the precision of common tracking algorithms, see Cheezum et al. 2001).

The quality of the measurement of an object can be characterized in terms of the signal-to-noise ratio (SNR). Because of the low background noise of our APD measurements, the noise (σ) in the images was, to a very good approximation, the noise of the object intensity itself. A good SNR estimate is therefore

$$\mathrm{SNR} = \frac{I_0}{\sigma_{\mathrm{sig}}}, \tag{1}$$

where I_0 is the mean intensity signal amplitude above the mean background signal I_B and σ_{sig} gives the standard deviation of the intensity signal. Localizing a fluorescent object and simultaneously determining its shape and size requires that the tracking algorithm accounts for both the center of the intensity distribution $I_{sig}(x,y)$ and its particular shape. Precise detection of the edges of an object requires accurate interpolation of the two-dimensional intensity distribution, in particular a satisfactory interpolation of the lower intensity values at the edges of the distribution (see below). To characterize the fluctuations in the fluorescence signal $I_{sig}(x,y)$, its standard deviation,

$$\sigma_{\mathrm{sig}} = \sqrt{\frac{\sum_{(i,j)\in\mathcal{M}_{\mathrm{obj}}} \left[I_{\mathrm{sig}}(i,j) - \bar{I}_{\mathrm{sig}}(i,j)\right]^2}{\mathrm{card}\left(\mathcal{M}_{\mathrm{obj}}\right) - 1}}, \tag{2}$$

can be estimated, where card $(\mathcal{M}_{obj})$ is the cardinal number of the set

$$\mathcal{M}_{\mathrm{obj}} = \left\{(i,j) \in x \times y | \bar{I}_{\mathrm{sig}}(x,y) \geqslant 10^{-2} \times I_0\right\}, \tag{3}$$

in other words the number of elements in $\mathcal{M}_{obj}$. A good estimate of the average intensity $\bar{I}_{sig}(x,y)$ can be obtained by fitting (χ^2- minimization) a theoretical intensity distribution $\mathcal{I}_{obj}(x,y)$ to the fluorescence image of the object (see below). The amplitude of $\mathcal{I}_{obj}(x,y)$ above the background I_B (the background constant I_B serves as an additional free fit parameter) further provides an estimate for the mean signal amplitude I_0 (see Eq. 1). The definition of the set $\mathcal{M}_{obj}$ guarantees that the computer algorithm only takes into account pixels that belong to the object. The SNR calculated in the suggested way is thus a measure of the quality of the object intensity only.

Theory

Recovery of shape, size, orientation and position of *E. coli* from fluorescence images by convolution analysis

The idea of this approach is to fit a theoretical intensity distribution of a finite model object such as a bacterium to a measured fluorescence image of the bacterium in order to obtain its position, orientation, shape and size. This result is achieved in three steps. First, a geometrical model of the bacterium must be assumed. Second, an expression for the fluorescence image resulting from this model must be derived. This expression contains all of the parameters for the bacterium's position, orientation, size and shape as free parameters. Third, the theoretical image is fitted to the experimental image (the parameters of the model are varied until the deviation of the former from the latter is minimized). In the following, steps one and two are discussed.

The most plausible way of modeling the geometry of an *E. coli* bacterium (Fig. 3a, inset) is by assuming a cylinder with two hemiellipsoidal caps attached to it (a "sausage model", Fig. 3a). If such an entity has homo-

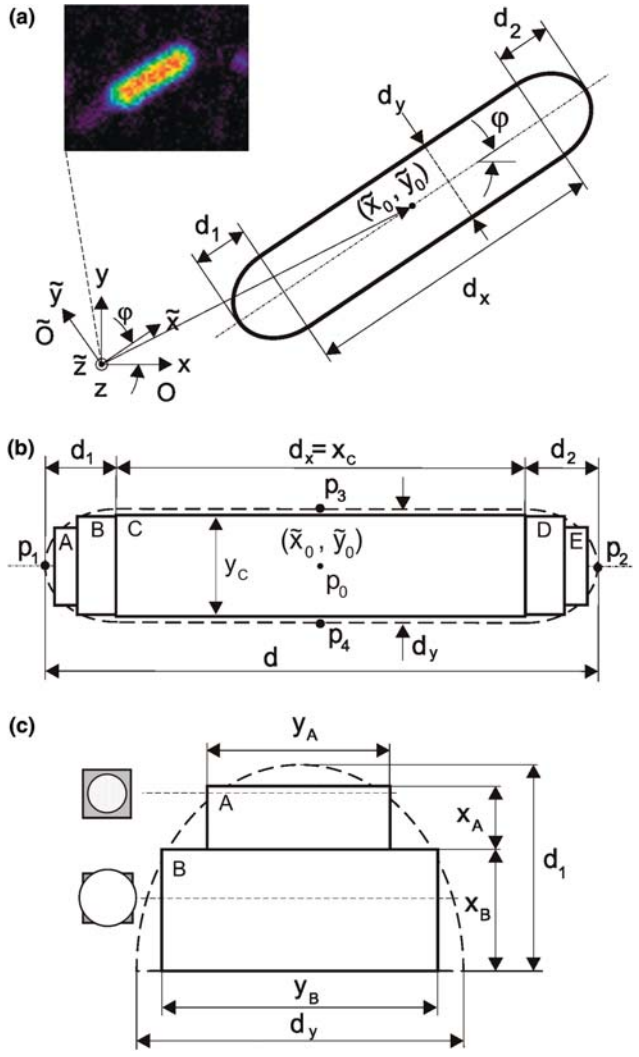

Fig. 3a–c Schematic representation of the three-dimensional "sausage model" and its approximation by a "slice model". **a** The position of the object within an image is defined by the coordinates $(\tilde{x}_0, \tilde{y}_0)$ given in the rotated coordinate system $\tilde{O}$, where its orientation is defined by the angle ϕ with respect to the x-axis of the coordinate system O. The positions of the center, the front end, the rear end, the right border and the left border of the approximated sausage model are given by the points p_0, p_1, p_2, p_3 and p_4, respectively, as indicated in (b) of this figure. *Inset*: CLSM images of an *E. coli* bacterium, stained with MitoTracker Orange. Image size: 61×51 pixels; pixel size: 89 nm; pixel dwell time: 3.45 µs. **b** "Slice model". Approximation of the sausage model by a stack of five rectangular slices and their geometrical parameters. **c** Detail: approximation of a hemi-ellipsoidal cap by two slices. For further details, see text

geneously accumulated a fluorescent dye of concentration $\langle C \rangle$, the resulting fluorescence image is given by

$$I_{\mathrm{obj}}(x,y) = \langle C \rangle \int_{-\infty}^{+\infty} \mathrm{d}x' \int_{-\infty}^{+\infty} \mathrm{d}y' \int_{-\infty}^{+\infty} \mathrm{d}z' \chi_{\mathrm{obj}}(x',y',z') \times I_{\mathrm{E}}(x-x', y-y', z'), \tag{4}$$

in which $I_{\mathrm{obj}}(x,y)$ is the convolution product of the "characteristic" object function $\chi_{\mathrm{obj}}(x',y',z')$ (which is unity at all points of the fluorescent object and otherwise zero, Gennerich and Schild 2002), with the function describing the three-dimensional Gaussian volume from which the emission intensity is detected, the so-called detectable emission intensity distribution $I_{\mathrm{E}}(x,y,z)$ (Rigler et al. 1993),

$$I_{\mathrm{E}}(x,y,z) = gQI_a \mathrm{e}^{-2\left[\left(x^2+y^2\right)/r_{xy}^2\right]} \mathrm{e}^{-l\left(z^2/r_z^2\right)}. \tag{5}$$

g accounts for the overall optical losses of the emission pathway, including the efficiency of the APD, and Q is the quantum efficiency of the fluorescent dye. I_{a} is the maximum laser intensity in the focus. As the object under investigation may have any orientation with respect to the coordinate system, we rotate the coordinate system around the z-axis by the angle ϕ,

$$\tilde{x} = x\cos\varphi + y\sin\varphi \tag{6}$$

$$\tilde{y} = y\cos\varphi - x\sin\varphi, \tag{7}$$

so that the major symmetry axis of the object coincides with the $\tilde{x}$-axis of the coordinate system $\tilde{O}$ (Fig. 3a). The function describing the object, $\chi_{\mathrm{obj}}(x',y',z')$, is then, due to its symmetry (see Fig. 3a), conveniently expressed in cylinder coordinates, x',r,θ:

$$\begin{aligned}\chi_{\mathrm{obj}}(x',r,\theta) &= \chi_{[\tilde{x}_0-d_1-d_x/2,\tilde{x}_0-d_x/2]}(x') \\ &\quad \times \chi_{\left[0,(d_y/2)\{1-(x'-\tilde{x}_0+d_x/2)^2/d_1^2\}^{1/2}\right]}(r) \\ &\quad + \chi_{[\tilde{x}_0-d_x/2,\tilde{x}_0+d_x/2]}(x') \times \chi_{[0,d_y/2]}(r) \\ &\quad + \chi_{[\tilde{x}_0+d_x/2,\tilde{x}_0+d_x/2+d_2]}(x') \\ &\quad \times \chi_{\left[0,(d_y/2)\{1-(x'-\tilde{x}_0-d_x/2)^2/d_2^2\}^{1/2}\right]}(r) \\ &= \chi_{\mathrm{obj}}(x',r)\end{aligned} \tag{8}$$

using the characteristic function

$$\chi_{[a,b]}(\gamma) = \begin{cases} 1 & \text{for } a \leqslant \gamma \leqslant b \\ 0 & \text{otherwise.} \end{cases} \tag{9}$$

Equation 8 has three parts, describing the first ellipsoidal cap of the bacterium, the cylindrical middle piece, and the second cap, respectively. Rewriting Eq. 4 using the coordinate transformations $x' = x'$, $y' = r\cos\theta + \tilde{y}_0$ and $z' = r\sin\theta$, and substituting Eqs. 5 and 8 leads to the three expected intensity contributions of the first cap, the shaft, and the second cap of the bacterium:

$$\begin{aligned} I_{\mathrm{obj}}(\tilde{x},\tilde{y}) &= \langle C \rangle \int_{-\infty}^{+\infty} \mathrm{d}x' \int_{0}^{+\infty} \mathrm{d}r \int_{0}^{2\pi} \mathrm{d}\theta r \times \chi_{\mathrm{obj}}(x',r) \\ &\quad \times I_{\mathrm{E}}(\tilde{x}-x', \tilde{y}-\tilde{y}_0 - r\cos\theta, r\sin\theta) \\ &= I_{\mathrm{obj}}^{\mathrm{ell1}}(\tilde{x},\tilde{y}) + I_{\mathrm{obj}}^{\mathrm{cyl}}(\tilde{x},\tilde{y}) + I_{\mathrm{obj}}^{\mathrm{ell2}}(\tilde{x},\tilde{y}) \end{aligned} \tag{10}$$

(the full derivations for $I_{\mathrm{obj}}^{\mathrm{ell1}}(\tilde{x},\tilde{y})$, $I_{\mathrm{obj}}^{\mathrm{cyl}}(\tilde{x},\tilde{y})$ and $I_{\mathrm{obj}}^{\mathrm{ell2}}(\tilde{x},\tilde{y})$ are given in Appendix A).

Although it is feasible to use Eq. 10 along with the coordinate transformation (Eqs. 6 and 7) as the function to be fitted to an experimental image, it is rather time-consuming due to the numerical evaluation of integrals, at least on a standard personal computer. Should one try to use Eq. 10 to calculate the cross-correlation functions (see below), this problem would become even more serious. As an example, fitting Eq. 10 to an experimental image of a fluorescent *E. coli* of 100×64 pixels takes three hours on a PC with a Pentium III processor.

We therefore derived an alternative model that allows much faster evaluation. We approximate the bacterium by a stack of five rectangular slices, A through E, as shown in Fig. 3b. For every slice, the length x_U, width y_U and height $z_U = y_U$, with $U \in \mathcal{M} = \{A, B, C, D, E\}$, were obtained by setting two conditions. First, the total volume of the sausage and slice models must be equal. This guarantees the same number of photon-emitting molecules. Second, we required that the portion of the slice volume situated outside the sausage (Fig. 3c, see gray areas of the cross-sections drawn) be minimized. For the sake of simplicity, prior to carrying out the optimization procedure, we decomposed the sausage model into three parts and approximated each part separately (the hemiellipsoidal caps by two slices each and the cylinder by one slice only). For the hemiellipsoidal caps, the optimization cannot be solved analytically. However, the equation of the volume of the two slices situated outside the cap can easily be derived and its minimum can be found numerically using, for instance, Mathematica (Wolfram Research, Champain, IL, USA). Carrying out this optimization, all of the parameters x_U, y_U and $z_U = y_U$, with $U \in \mathcal{M}$, can be formulated as a function of the underlying object parameters d_1, d_2 and d_y only (see Appendix B).

Using a stack of slices aids all subsequent calculations considerably, because the integration variables x', y' and z' of Eq. 4 now become separable. Evaluating Eq. 4 with a proper object function describing the slice model leads to

$$\begin{aligned}\mathcal{I}_{\mathrm{obj}}(\tilde{x},\tilde{y}) &= \sum_{U\in M} \mathcal{I}_U(\tilde{x},\tilde{y}) \\ &= \mathcal{I}_{\mathrm{A}}(\tilde{x},\tilde{y}) + \mathcal{I}_{\mathrm{B}}(\tilde{x},\tilde{y}) + \mathcal{I}_{\mathrm{C}}(\tilde{x},\tilde{y}) \\ &\quad + \mathcal{I}_{\mathrm{D}}(\tilde{x},\tilde{y}) + \mathcal{I}_{\mathrm{E}}(\tilde{x},\tilde{y}), \end{aligned} \tag{11}$$

where $\mathcal{I}_U(\tilde{x},\tilde{y})$, $U \in \mathcal{M}$, are given in Appendix C. The five terms of this expression give the intensity contributions from the five slices of the model. Following the substitutions of the Eqs. 6, 7, 38 and 39 of the coordinate and parameter transformations into the derived Eq. 11, this function can be directly fitted to an experimental fluorescence image yielding the parameters describing the position, orientation, shape and size of the object. By varying the parameters d_1, d_2, d_x and d_y of the underlying model, the object can easily assume the shape of a sausage, cigar, ellipsoid or sphere.

Recovery of shape, size, orientation and position of *E. coli* from fluorescence images by correlation analysis

Consider a microscope image of a homogeneously-stained bacterium (Fig. 4a). How can the parameters for its position, orientation, shape and size be obtained by correlation analysis? We will derive an algorithm that makes use of both autocorrelation and cross-correlation image analysis. In the first step, the ACFs of the individual images are analyzed to obtain, for each image, the orientation, shape, and size parameters of the object of interest. This information is then used to calculate a template for each experimental image. Second, the cross-correlation functions (CCF) of the subsequent templates and images are calculated and analyzed to obtain the positions of the object in the subsequent images and to re-evaluate the shape and size parameters of the object of interest (see below).

The experimental ACF of the image under consideration (Fig. 4a) is shown in Fig. 4b. To obtain the orientation, shape and size parameters of the object, we calculated the ACF, $G(\xi,\eta)$, of the intensity distribution, $\mathcal{I}(x,y)$, of the slice model (Eq. 11 with Eqs. 6 and 7), in other words

$$G(\xi,\eta) = \frac{\langle \mathcal{I}(x,y)\mathcal{I}(x+\xi,y+\eta)\rangle}{\langle \mathcal{I}(x,y)\rangle^2} = \frac{G'(\xi,\eta)}{\langle \mathcal{I}(x,y)\rangle^2}, \tag{12}$$

where $G'(\xi,\eta)$ is the unnormalized ACF. The angular brackets,$\langle\rangle$, indicate integration over space (Petersen et al. 1993). As the resulting ACF contains all free parameters to be obtained, fitting $G(\xi,\eta)$ to the experimental ACF (Fig. 4b) yields the free parameters, in particular the angle ϕ by which the bacterium is rotated with respect to the x-axis. (Obviously the position of the object cannot be retrieved in this way.) The noise components of the original image give rise to a peak at the origin of the ACF (barely seen in Fig. 4b). The width of the peak depends on the noise spectrum of the image and in any case affects the accuracy of the calculated shape and size parameters. Before evaluating the ACF, we therefore replaced the central peak by an "appropriate" value. This was achieved in three steps. First, the central value was replaced by the mean of the nearest neighbors. Second, a 2-D Gaussian distribution was fitted to the ACF center and its four nearest neighbors (Cheezum et al. 2001), and third, the central ACF value was replaced by the maximum of the fitted Gaussian distribution.

Finally, the parameters obtained from the ACF fit were used to generate a template of the bacterium centered at the middle of an image (Fig. 4c).

The next step was to calculate the CCF of the original image (Fig. 4a) and the template (Fig. 4c), as shown in Fig. 4d. To obtain the shape and position parameters of the object, this "experimental" CCF needs to be fitted using a model CCF that contains these parameters. Therefore, we calculate the theoretical CCF of the in-

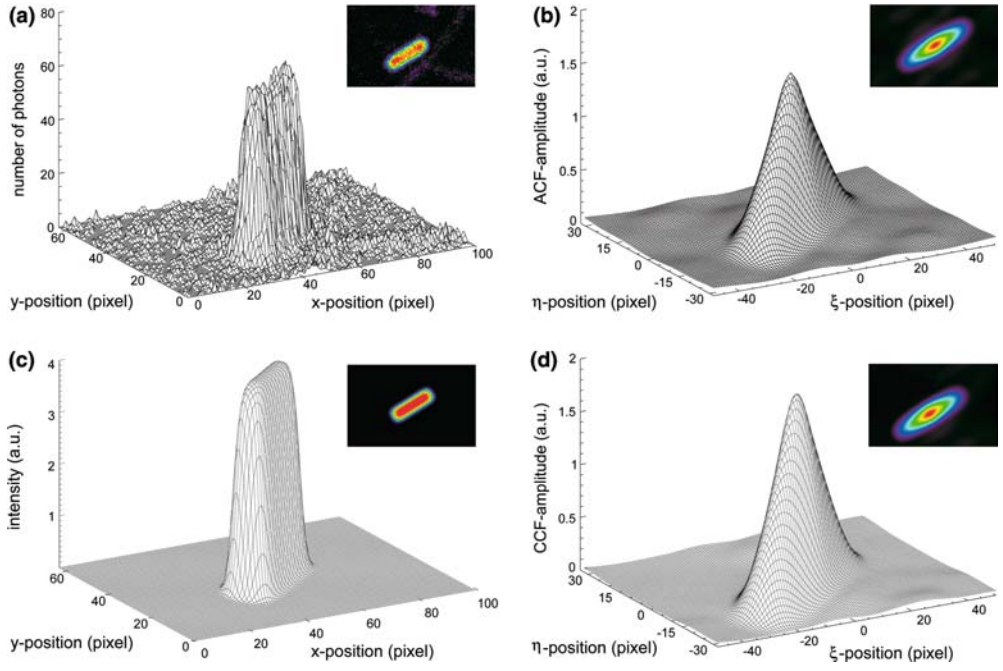

Fig. 4a–c Correlation image analysis. **a** Intensity distribution of an *E. coli* bacterium, stained with MitoTracker Orange. The corresponding CLSM-image is shown in the inset. Image size: 100×64 pixels ; pixel size: 88 nm; scan time per frame: 64.64 ms. **b** ACF of the image shown in (a). Fitting the theoretical ACF $G(\xi,\eta)$ (Eq. 33 together with Eqs. 6 and 7, with $d_1^{(1)}=d_1^{(2)}$, $d_2^{(1)}=d_2^{(2)}$, $d_x^{(1)}=d_x^{(2)}$ and $d_y^{(1)}=d_y^{(2)}$) gave: $d_x=2196.7$ nm, $d_1=576$ nm, $d_2=448.2$ nm, $d_y=1001.2$ nm and $\phi=0.556$. These data result in an *E. coli* length of $d=d_1+d_x+d_2=3220.8$ nm. **c** Template for the *E. coli* bacterium; in other words the intensity distribution $\mathcal{I}_{\mathrm{obj}}(x,y)$ (Eq. 11 with Eqs. 6, 7, 38 and 39) of the slice model calculated using the parameters obtained from the ACF analysis. **d** CCF of the CLSM image shown in (a) and its template shown in (c)

tensity distribution $\mathcal{I}^{(1)}(x,y)$ of a slice model with free parameters, and the template , $\mathcal{I}^{(2)}(x,y)$,

$$G'(\xi,\eta)=\left\langle \mathcal{I}^{(1)}(x,y)\mathcal{I}^{(2)}(x+\xi,y+\eta)\right\rangle. \tag{13}$$

As the template derived from the object image and the object itself have the same orientation ϕ with respect to the x-axis (Fig. 5), we can start out to derive the CCF $G'\left(\tilde{\xi},\tilde{\eta}\right)$ as given in the rotated system $\tilde{\mathcal{O}}$. As above, the slice model images comprise the intensity distributions of the five slices A, B, C, D, and E, in other words

$$\mathcal{I}^{(1)}_{\mathrm{obj}}(\tilde{x},\tilde{y})=\sum_{U\in\mathcal{M}}\mathcal{I}^{(1)}_{U}(\tilde{x},\tilde{y}) \tag{14}$$

$$\mathcal{I}^{(2)}_{\mathrm{obj}}(\tilde{x},\tilde{y})=\sum_{V\in\mathcal{M}}\mathcal{I}^{(2)}_{V}(\tilde{x},\tilde{y}), \tag{15}$$

so that the theoretical CCF is a sum of 25 terms,

$$G'\left(\tilde{\xi},\tilde{\eta}\right)=\sum_{U,V\in\mathcal{M}}G'_{UV}\left(\tilde{\xi},\tilde{\eta}\right), \tag{16}$$

with

$$G'_{UV}\left(\tilde{\xi},\tilde{\eta}\right)=\int_{-\infty}^{+\infty}\int_{-\infty}^{+\infty}\mathrm{d}\tilde{x}\,\mathrm{d}\tilde{y}\,\mathcal{I}^{(1)}_{U}(\tilde{x},\tilde{y})\mathcal{I}^{(2)}_{V}\left(\tilde{x}+\tilde{\xi},\tilde{y}+\tilde{\eta}\right). \tag{17}$$

As an example, let us consider the two central slices of the models and their contribution to the CCF. After substituting the object functions of the central portions (Fig. 5),

$$\begin{aligned}\chi^{(1)}_{\mathrm{C}}(x',y',z')=&\,\chi_{[\tilde{x}_0^{(1)}-\tilde{x}_{\mathrm{C}}^{(1)}/2,\tilde{x}_0^{(1)}+\tilde{x}_{\mathrm{C}}^{(1)}/2]}(x')\\&\times\chi_{[\tilde{y}_0^{(1)}-\tilde{y}_{\mathrm{C}}^{(1)}/2,\tilde{y}_0^{(1)}+\tilde{y}_{\mathrm{C}}^{(1)}/2]}(y')\\&\times\chi_{[-\tilde{z}_{\mathrm{C}}^{(1)}/2,\tilde{z}_{\mathrm{C}}^{(1)}/2]}(z')\end{aligned} \tag{18}$$

and

$$\begin{aligned}\chi^{(2)}_{\mathrm{C}}(x'',y'',z'')=&\,\chi_{[\tilde{x}_0^{(2)}-\tilde{x}_{\mathrm{C}}^{(2)}/2,\tilde{x}_0^{(2)}+\tilde{x}_{\mathrm{C}}^{(2)}/2]}(x'')\\&\times\chi_{[\tilde{y}_0^{(2)}-\tilde{y}_{\mathrm{C}}^{(2)}/2,\tilde{y}_0^{(2)}+\tilde{y}_{\mathrm{C}}^{(2)}/2]}(y'')\\&\times\chi_{[-\tilde{z}_{\mathrm{C}}^{(2)}/2,\tilde{z}_{\mathrm{C}}^{(2)}/2]}(z'')\end{aligned} \tag{19}$$

into Eq. 4, we get the respective images of slices C,

$$\begin{aligned}\mathcal{I}^{(1)}_{\mathrm{C}}(\tilde{x},\tilde{y})=&\,q_1\sqrt{\frac{\pi}{2}}r_z\mathrm{erf}\left(\frac{z^{(1)}_{\mathrm{C}}}{\sqrt{2}r_z}\right)\\&\times\int_{\tilde{x}_0^{(1)}-\tilde{x}_{\mathrm{C}}^{(1)}/2}^{\tilde{x}_0^{(1)}+\tilde{x}_{\mathrm{C}}^{(1)}/2}\mathrm{d}x'\int_{\tilde{y}_0^{(1)}-\tilde{y}_{\mathrm{C}}^{(1)}/2}^{\tilde{y}_0^{(1)}+\tilde{y}_{\mathrm{C}}^{(1)}/2}\mathrm{d}y'\mathrm{e}^{-2\left[(\tilde{x}-x')/r_{xy}^2\right]}\mathrm{e}^{-2\left[(\tilde{y}-y')/r_{xy}^2\right]}\end{aligned} \tag{20}$$

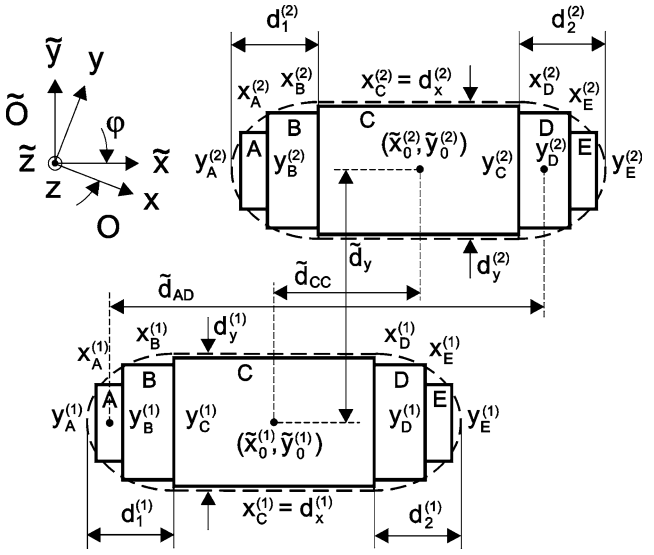

Fig. 5 Schematic representations and parameters of two displaced slice models. Both objects have the same orientation with respect to the x-axis of the coordinate system O. The intensity distributions of the objects are denoted by $\mathcal{I}_{\mathrm{obj}}^{(1)}(\tilde{x},\tilde{y})$ and $\mathcal{I}_{\mathrm{obj}}^{(2)}(\tilde{x},\tilde{y})$, respectively

$$\mathcal{I}_{\mathrm{C}}^{(2)}(\tilde{x},\tilde{y}) = q_2\sqrt{\frac{\pi}{2}}r_z\mathrm{erf}\left(\frac{z_{\mathrm{C}}^{(2)}}{\sqrt{2}r_z}\right)\int\limits_{\tilde{x}_0^{(2)}-\tilde{x}_{\mathrm{C}}^{(2)}/2}^{\tilde{x}_0^{(2)}+\tilde{x}_{\mathrm{C}}^{(2)}/2}\mathrm{d}x'' \times\int\limits_{\tilde{y}_0^{(2)}-\tilde{y}_{\mathrm{C}}^{(2)}/2}^{\tilde{y}_0^{(2)}+\tilde{y}_{\mathrm{C}}^{(2)}/2}\mathrm{d}y''\mathrm{e}^{-2\left[(\tilde{x}-x'')/r_{xy}^2\right]}\mathrm{e}^{-2\left[(\tilde{y}-y'')/r_{xy}^2\right]}, \tag{21}$$

where $q_1 = gQI_{\mathrm{a}}\langle C_1\rangle$ and $q_2 = gQI_{\mathrm{a}}\langle C_2\rangle$, with $\langle C_1\rangle$ and $\langle C_2\rangle$ being the respective dye concentrations in the slice models. Substituting Eqs. 20 and 21 into Eq. 17 results in the CCF component of these slices,

$$\begin{aligned}G'_{\mathrm{CC}}\left(\tilde{\xi},\tilde{\eta}\right) = {} & q_1q_2\frac{\pi^3}{27}r_{xy}^4r_z^2x_{\mathrm{C}}^{(2)}y_{\mathrm{C}}^{(2)}\mathrm{erf}\left(\frac{z_{\mathrm{C}}^{(1)}}{\sqrt{2}r_z}\right)\mathrm{erf}\left(\frac{z_{\mathrm{C}}^{(2)}}{\sqrt{2}r_z}\right)\\ & \times\int\limits_{-1}^{1}\mathrm{d}x''\left[\mathrm{erf}\left(\frac{\tilde{\xi}-\tilde{d}_{\mathrm{CC}}-x''\left[x_{\mathrm{C}}^{(2)}/2\right]+\left[x_{\mathrm{C}}^{(1)}/2\right]}{r_{xy}}\right)\right.\\ & \left.-\mathrm{erf}\left(\frac{\tilde{\xi}-\tilde{d}_{\mathrm{CC}}-x''\left[x_{\mathrm{C}}^{(2)}/\right]-\left[x_{\mathrm{C}}^{(1)}/2\right]}{r_{xy}}\right)\right]\\ & \times\int\limits_{-1}^{1}\mathrm{d}y''\left[\mathrm{erf}\left(\frac{\tilde{\eta}-\tilde{d}_y-y''\left[y_{\mathrm{C}}^{(2)}/2\right]+\left[y_{\mathrm{C}}^{(1)}/2\right]}{r_{xy}}\right)\right.\\ & \left.-\mathrm{erf}\left(\frac{\tilde{\eta}-\tilde{d}_y-y''\left[y_{\mathrm{C}}^{(2)}/2\right]-\left[y_{\mathrm{C}}^{(1)}/2\right]}{r_{xy}}\right)\right],\end{aligned} \tag{22}$$

with $\tilde{d}_{\mathrm{CC}} = \tilde{x}_0^{(2)} - \tilde{x}_0^{(1)}$ and $\tilde{d}_y = \tilde{y}_0^{(2)} - \tilde{y}_0^{(1)}$. Finally, this equation can be reduced to an equation that requires the calculation of exponential and error functions only:

$$\begin{aligned}G'_{\mathrm{CC}}\left(\tilde{\xi},\tilde{\eta}\right) = {} & q_1q_2\frac{\pi^{5/2}}{2^5}r_{xy}^5r_z^2\mathrm{erf}\left(\frac{z_{\mathrm{C}}^{(1)}}{\sqrt{2}r_z}\right)\mathrm{erf}\left(\frac{z_{\mathrm{C}}^{(2)}}{\sqrt{2}r_z}\right)\\ & \times\sum_{\varepsilon_1,\varepsilon_2\in\{\pm1\}}\varepsilon_1\varepsilon_2\left\{\exp\left[-\mathcal{A}(\varepsilon_1,\varepsilon_2)^2\Big/r_{xy}^2\right]\right.\\ & \left.+\frac{\sqrt{\pi}}{r_{xy}}\mathcal{A}(\varepsilon_1,\varepsilon_2)\mathrm{erf}\left[\mathcal{A}(\varepsilon_1,\varepsilon_2)/r_{xy}\right]\right\}\\ & \times\sum_{\varepsilon_1,\varepsilon_2\in\{\pm1\}}\varepsilon_1\varepsilon_2\left\{\exp\left[-\mathcal{B}(\varepsilon_1,\varepsilon_2)^2\Big/r_{xy}^2\right]\right.\\ & \left.+\frac{\sqrt{\pi}}{r_{xy}}\mathcal{B}(\varepsilon_1,\varepsilon_2)\mathrm{erf}\left[\mathcal{B}(\varepsilon_1,\varepsilon_2)/r_{xy}\right]\right\}\end{aligned}, \tag{23}$$

where

$$\mathcal{A}(\varepsilon_1,\varepsilon_2) = \left(\tilde{\xi}-\tilde{d}_{\mathrm{CC}}+\varepsilon_1\frac{x_{\mathrm{C}}^{(1)}}{2}+\varepsilon_2\frac{x_{\mathrm{C}}^{(2)}}{2}\right) \tag{24}$$

$$\mathcal{B}(\varepsilon_1,\varepsilon_2) = \left(\tilde{\eta}-\tilde{d}_y+\varepsilon_1\frac{y_{\mathrm{C}}^{(1)}}{2}+\varepsilon_2\frac{y_{\mathrm{C}}^{(2)}}{2}\right). \tag{25}$$

The other 24 terms of the CCF $G'\left(\tilde{\xi},\tilde{\eta}\right)$ (Eq. 16) can be obtained from Eq. 23 by using the appropriate slice distances. For example, for the case of the CCF component resulting from the intensity distributions of slice A of the first object and slice D of the second one (see Fig. 5),

$$\tilde{d}_{\mathrm{AD}} = \tilde{d}_{\mathrm{CC}}+\frac{x_{\mathrm{C}}^{(1)}}{2}+x_{\mathrm{B}}^{(1)}+\frac{x_{\mathrm{A}}^{(1)}}{2}+\frac{x_{\mathrm{C}}^{(2)}}{2}+\frac{x_{\mathrm{D}}^{(2)}}{2}. \tag{26}$$

By expressing the distances of the slices in the suggested way, the parameter $\tilde{d}_{\mathrm{CC}}$ will serve as the only parameter that accounts for the displacement between both slice models along the $\tilde{x}$-axis. The parameter $\tilde{d}_y$, describing the displacement between both models with respect to the $\tilde{y}$-axis, is identical for all slices A through E and does not need to be replaced. Finally, the size parameters $x_{\mathrm{C}}^{(1)}$, $x_{\mathrm{C}}^{(2)}$, $y_{\mathrm{C}}^{(1)} = z_{\mathrm{C}}^{(1)}$ and $y_{\mathrm{C}}^{(2)} = z_{\mathrm{C}}^{(2)}$ have to be replaced by the corresponding parameters $x_{\mathrm{A}}^{(1)}$, $x_{\mathrm{D}}^{(2)}$, $y_{\mathrm{A}}^{(1)} = z_{\mathrm{A}}^{(1)}$ and $y_{\mathrm{D}}^{(2)} = z_{\mathrm{D}}^{(2)}$ of the slices A and D of the models.

Up to this point we have used the unnormalized CCF $G'\left(\tilde{\xi},\tilde{\eta}\right)$ (Eq. 16). The normalized CCF $G\left(\tilde{\xi},\tilde{\eta}\right)$ is given by

$$G\left(\tilde{\xi},\tilde{\eta}\right) = \frac{\sum_{U,V\in\mathcal{M}}G'_{UV}\left(\tilde{\xi},\tilde{\eta}\right)}{\sum_{U,V\in\mathcal{M}}\left\langle\mathcal{I}_U^{(1)}(\tilde{x},\tilde{y})\right\rangle\left\langle\mathcal{I}_V^{(2)}(\tilde{x},\tilde{y})\right\rangle} \tag{27}$$

with

$$\left\langle \mathcal{I}_U^{(i)}(\tilde{x},\tilde{y})\right\rangle = \int_{-\infty}^{+\infty}\int_{-\infty}^{+\infty} \mathrm{d}\tilde{x}\,\mathrm{d}\tilde{y}\mathcal{I}_U^{(i)}(\tilde{x},\tilde{y}) = q_i\left(\frac{\pi}{2}\right)^{3/2} r_{xy}^2 r_z x_U^{(i)} y_U^{(i)} \mathrm{erf}\left[z_U^{(i)}\Big/\left(\sqrt{2}r_z\right)\right], \tag{28}$$

($i=1,2$) and thus

Using the definitions

$$G(\tilde{\xi},\tilde{\eta}) = \frac{\sum_{U,V\in\mathcal{M}} G'_{UV}(\tilde{\xi},\tilde{\eta})}{q_1 q_2 \frac{\pi^3}{8} r_{xy}^4 r_z^2 \sum_{U,V\in\mathcal{M}} x_U^{(1)} x_V^{(2)} y_U^{(1)} y_V^{(2)} \mathrm{erf}\left[z_U^{(1)}\Big/\left(\sqrt{2}r_z\right)\right]\mathrm{erf}\left[z_V^{(2)}\Big/\left(\sqrt{2}r_z\right)\right]}. \tag{29}$$

$$g'_{UV}\left(\tilde{\xi},\tilde{\eta}\right) = \frac{2^5}{q_1 q_2 \pi^{(5/2)} r_{xy}^5 r_z^2} G'_{UV}\left(\tilde{\xi},\tilde{\eta}\right) \tag{30}$$

and

$$G_0 = \frac{r_{xy}}{4\sqrt{\pi}}\left(\sum_{U,V\in\mathcal{M}} x_U^{(1)} x_V^{(2)} y_U^{(1)} y_V^{(2)} \mathrm{erf}\left[z_U^{(1)}\Big/\left(\sqrt{2}r_z\right)\right] \times \mathrm{erf}\left[z_V^{(2)}\Big/\left(\sqrt{2}r_z\right)\right]\right)^{-1}, \tag{31}$$

simplifies the expression for $G\left(\tilde{\xi},\tilde{\eta}\right)$,

$$G\left(\tilde{\xi},\tilde{\eta}\right) = G_0 \sum_{U,V\in\mathcal{M}} g'_{UV}\left(\tilde{\xi},\tilde{\eta}\right). \tag{32}$$

This CCF does not depend on the constants $q_1 = gQI_a\langle -C_1\rangle$ and $q_2 = gQI_a\langle C_2\rangle$ because the constants cancel in Eq. 30. Evaluating normalized experimental correlation functions is therefore useful if the ACFs and CCFs of images of objects with different dye concentrations are to be compared. With the factor G_0 as an additional fit parameter, however, $G\left(\tilde{\xi},\tilde{\eta}\right)$ (Eq. 32) can be used together with the coordinate and parameter transformations (Eqs. 6, 7, 38 and 39) to analyze both experimental unnormalized and normalized ACFs and CCFs.

Finally, we must account for the fact that all experimental images show some background noise around the actual object, leading to non-zero offsets in the experimental ACF and CCF, respectively (Fig. 4b, d). The model CCF obviously does not include such noise. To fit the model CCF to the data CCF we therefore add a constant term g_B to the CCF derived above to account for this offset:

$$G(\xi,\eta) = g_B + G_0 \sum_{U,V\in\mathcal{M}} g'_{UV}(\xi,\eta). \tag{33}$$

Results and discussion

Geometry choice for the *E. coli* model

Of the two models derived above (the sausage model and the slice model), algorithms using the slice model are markedly faster. However, the slice model can only be preferred if the error introduced by approximating the sausage model by slices is acceptable. As shown in Appendix D, the slice model gives reliable results when used to determine the absolute length of sausage-like objects such as *E. coli* bacteria, or when used to detect relative length and width changes. In the following analysis we therefore use the slice model.

The method of choice: convolution versus correlation analysis

Consider the *E. coli* shown in Fig. 4a, and an x-section through it at $y=30$ (Fig. 6a, noisy curve). The fluorescence intensity distribution of the slice model (Eq. 11 including Eqs. 6 and 7) is then fitted to the bacterium's image, and a section through the resulting function, $\mathcal{I}_{obj}(x,y)$, at $y=30$ is given by the continuous curve in Fig. 6a. Obviously, the question here is how well the size and the shape are approximated. Before answering this we applied the second method, using the auto- and cross-correlation functions as outlined in the "Theory" section. The continuous curve in Fig. 6b shows the experimental CCF resulting from the correlation of the original image and the template function (the template built via the ACF). On the other hand, the dashed curve of Fig. 6b is the model CCF calculated from a template with fixed parameters and a template with free parameters to be fitted. Fitting the model CCF $G(\xi,\eta)$ (Eq. 33 with Eqs. 6 and 7) to the experimental one yields the free parameters. The fit appears to follow the data in a satisfactory way. Here again the question is how well the bacterium's size and the shape are approximated.

It is intrinsically impossible to give an answer to this question relying only on calculations like those shown above. Instead one has to start out with an object of known geometrical parameters. The procedure for determining the precision of either algorithm using a known object is as follows. First, one deterministic image is generated by calculating the intensity $\mathcal{I}_{obj}(x,y)$ for a slice model (Eq. 11 with Eqs. 6 and 7) with zero background ($I_B=0$), assuming known, constant, and morphologically realistic *E.coli* parameters. We chose an object of ~3.2 μm length and ~1 μm width with its long axis parallel to the x-axis of the image, located at the center of the image (for parameters used, see legend of Fig. 7). Second, Poisson noise is added to the deterministic image so that the resulting test image has a well-known SNR (calculated according to Eq. 2), and third, this procedure is repeated for a number of images (here

$n = 100$). In this way we obtained a sequence of images of fluorescent objects, all with basically the same shape and size, with random noise superimposed, and with a constant mean SNR. Sets containing 100 images each were then generated for a number of different SNR values. To obtain the object parameters (see below) from 100 images of 96×30 pixels took the correlation algorithm ~50 hours on a PC with a Pentium III processor, whereas the convolution algorithm needed 30 minutes for the same task. We should point out that our implemented IDL algorithms were not optimized for fast image processing (so the use of thorough matrix-based image fitting algorithms would reduce the processing time markedly). Another future improvement will come from an increase in PC processor speed.

In the next step, the convolution and correlation methods were applied to each of the 100 images of a set, thereby resulting in 100 values per parameter and algorithm, as well as one average value and one standard deviation for each parameter. Here it is important to regard the precision and the accuracy of an algorithm separately. The standard deviation σ is a measure of the range within which a fitted parameter can fall, it describes the precision of the algorithm. The accuracy of both algorithms for detecting the characteristic object points $p_0(x)$, $p_0(y)$, $p_1(x)$, $p_2(x)$, $p_3(y)$, $p_4(y)$ (see Fig. 3b), the length d and the width d_y of the object, are obtained by calculating the bias of the detected parameters (the deviation of the mean values of the measured parameters from the known exact parameters). We then plotted σ and the bias of the object points, the length d and the width d_y as a function of the SNR ratio (Fig. 7a and b). The algorithms were applied as follows.

As described in the "Theory" section, the convolution method is based on fitting a theoretical intensity distribution of a model object to the measured image of the object of interest. Here, the intensity distribution $\mathcal{I}_{\mathrm{obj}}(x,y)$ (Eq. 11 with Eqs. 6 and 7) of the slice model was fitted to each of the successive simulated images. The free parameters to be fitted were the length $d_1 = d_2$ of the caps of the object, the length of the middle part d_x, the object's diameter d_y and the object's center $p_0 = (x_0, y_0)$ (Fig. 3b) (both the background constant $I_B = 0$ and the angle $\phi = 0$ were fixed). These parameters were then used to calculate the object points of interest.

The correlation method was applied as described above. First, the ACF of an image was calculated and its central peak at the origin was replaced by an appropriate value as outlined in the "Theory" section. The theoretical ACF (Eq. 33 with Eqs. 6 and 7) was then fitted to the resulting experimental ACF. The free parameters were the size parameters $d_1^{(1)} = d_1^{(2)} = d_2^{(1)} = d_2^{(2)}$, $d_x^{(1)} = d_x^{(2)}$ and $d_y^{(1)} = d_y^{(2)}$ of the object (see Fig. 5) (here, the displacement parameters $\tilde{d}_{\mathrm{CC}} = 0$ and $\tilde{d}_y = 0$, the background constant $g_B = 0$ and the angle $\phi = 0$ were fixed). The resulting object parameters were then used to calculate the intensity distribution $\mathcal{I}_{\mathrm{obj}}(x,y)$ of the template (see above). Second, the CCF of the template and the simulated image was fitted by the theoretical CCF $G(\xi,\eta)$ (Eq. 33 with Eqs. 6 and 7) to obtain the position of the object and to re-evaluate its size parameters. The free parameters were the parameters $d_1^{(1)} = d_2^{(1)}$, $d_x^{(1)}$, $d_y^{(1)}$ of the object and the displacement parameters $\tilde{d}_{\mathrm{CC}}$ and $\tilde{d}_y$. The parameters $d_1^{(2)} = d_2^{(2)}$, $d_x^{(2)}$ and $d_y^{(2)}$ of the template,

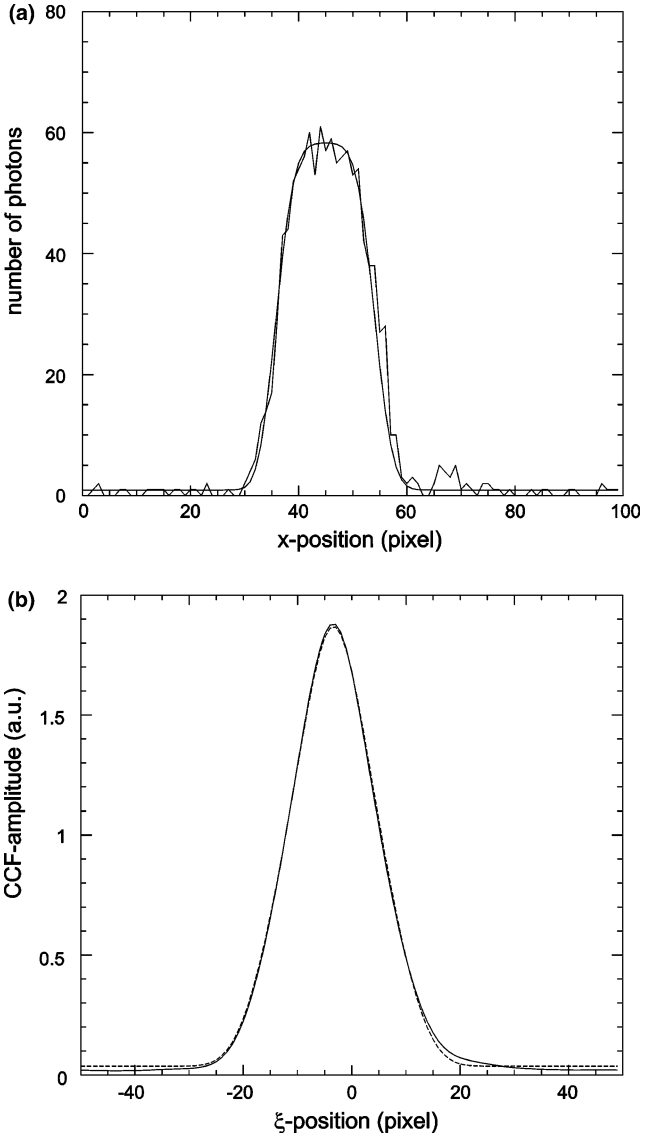

Fig. 6a–b Comparison of convolution and correlation analysis. **a** x-sections through the experimental intensity distribution of the *E. coli* bacterium shown in Fig. 4a (*noisy trace*) and through the fitted theoretical distribution $\mathcal{I}_{\mathrm{obj}}(x,y)$ (Eq. 11 with Eqs. 6, 7, 38 and 39) of the slice model (*smooth solid line*), both at $y = 30$. Result of the fit: $d_x = 2129.2$ nm, $d_1 = 664.6$ nm, $d_2 = 445.4$ nm, $d_y = 964.2$ nm and $\phi = 0.5609$ ($\chi^2 = 17946.66$). These data result in an *E. coli* length of $d = 3239.3$ nm. Fitting the intensity distribution $I_{\mathrm{obj}}(\tilde{x},\tilde{y})$ (Eq. 10 with Eqs. 6 and 7) of the sausage model gave: $d_x = 2152.7$ nm, $d_1 = 620.5$ nm, $d_2 = 467.4$ nm, $d_y = 1009.1$ nm and $\phi = 0.5611$ ($\chi^2 = 17190.81$). In this case, the *E. coli* length is $d = 3240.6$ nm. **b** ξ-sections through the maximum of the experimental CCF shown in Fig. 4d (*solid line*) and through the fitted theoretical CCF $G(\xi,\eta)$ (Eq. 33 with Eqs. 6 and 7, *dashed line*). Result of the fit: $d_x = 2186.8$ nm, $d_1 = 613.9$ nm, $d_2 = 428.6$ nm, $d_y = 1002.1$ nm and $\phi = 0.5558$ ($\chi^2 = 1.7759\times10^{-6}$). These data result in an *E. coli* length of $d = 3229.3$ nm

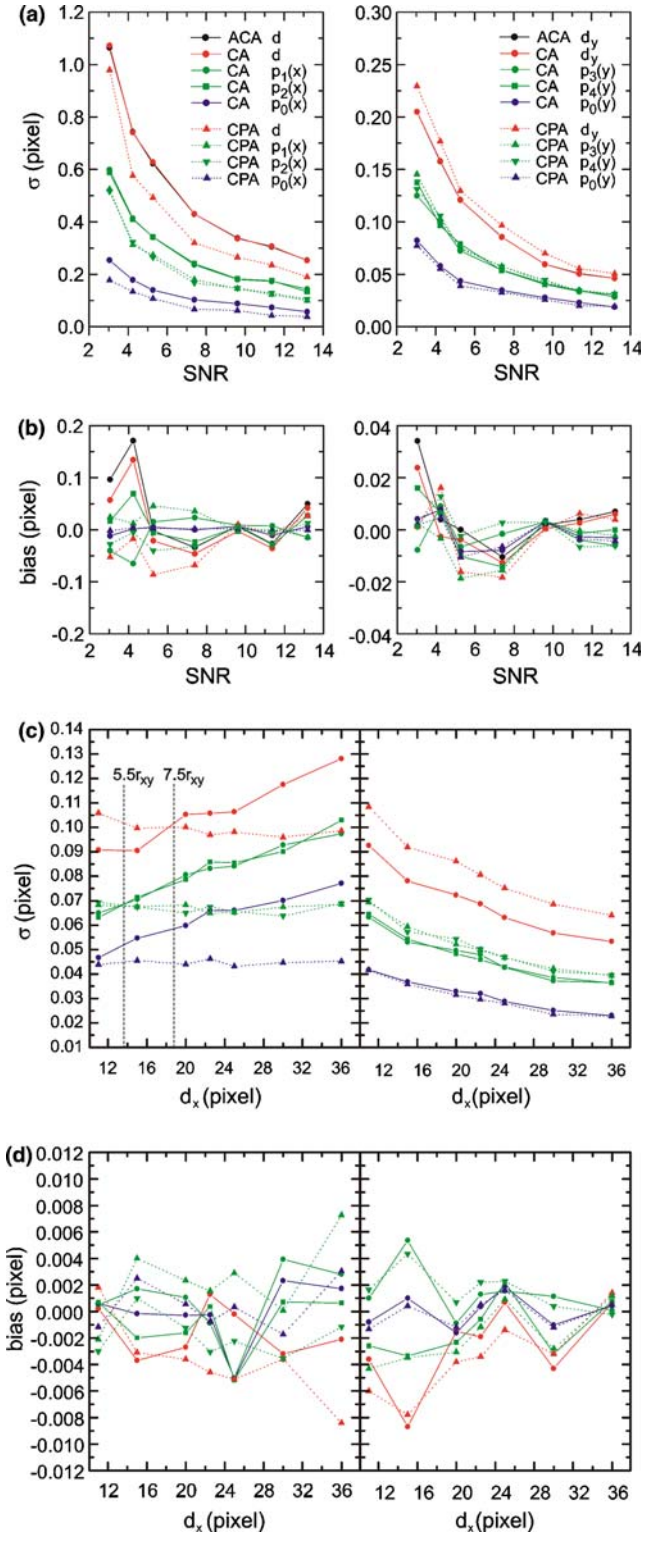

Fig. 7a–d Summary of precision and bias for the convolution and correlation algorithms analyzed by computer simulations (ACA: autocorrelation analysis; CA: correlation analysis; CPA: convolution product analysis). **a** Precision of both algorithms as a function of the SNR for determining the indicated parameters of the model object. Parameters used: $d_1 = d_2 = 5.5$ pixels, $d_x = 25$ pixels, $d_y = 11$ pixels and $\phi = 0$; pixel size: 88 nm; image size: 96×30 pixels (the corresponding bias of the measured parameters is shown in (b)). **b** Bias (deviation between the mean values of the measured parameters and the known exact parameters as a function of SNR). **c** Precision as a function of object size. Here, the underlying object was a box of length d_x and width $d_y = 11$. Its intensity distribution was calculated based on the intensity distribution $\mathcal{I}_{obj}(x, y)$ (Eq. 11 with $d_1 = d_2 = 0$) of the slice model. The mean SNR of the simulated images was 11. The image height was 30 pixels, whereas its width was adapted to the current box length d_x (the ratio of image height and box width d_y was equal to the ratio of image width and box length d_x for all images simulated). **d** Corresponding bias of the determined parameters as a function of box length d_x. The parameter names corresponding to the colored solid and dashed data traces shown left and right of (b), (c) and (d) are given on the left and right sides of (a) of this figure, respectively

the background constant $g_B = 0$ and the angle $\phi = 0$ were fixed. The characteristic object points p_0 to p_4 were then calculated based on the known position of the template and the resulting displacement and size parameters of the object.

The results of these calculations are shown in Fig. 7a and b, and can be summarized as follows:

1. The precision of either algorithm strongly increases (σ decreases) with increasing SNR
2. The object's diameter d_y can be determined more precisely than its length d (convolution analysis: 3.8-fold more precisely; correlation analysis: 5.3-fold)
3. The left and right borders $p_3(y)$ and $p_4(y)$ of the object are detected more precisely (smaller σ), than the front and rear end $p_1(x)$ and $p_2(x)$ (convolution analysis: 3.4-fold more precisely; correlation analysis: 4.6-fold)
4. The position of the object's center with respect to the y-axis ($p_0(y)$) can be determined more precisely than the object's center with respect to the x-axis ($p_0(x)$) (convolution analysis: 2.3-fold more precisely; correlation analysis: 3.1-fold)
5. The position of the object's center $p_0(x)$ can be detected more precisely than the positions $p_1(x)$ and $p_2(x)$ of the front end and rear end of the model (convolution analysis: 2.6-fold more precisely; correlation analysis: 2.3-fold), and the position of the object's center $p_0(y)$ can be determined more precisely than the positions $p_3(y)$ and $p_4(y)$ of the left and right border (convolution analysis: 1.8-fold more precisely; correlation analysis: 1.6-fold)
6. The convolution method results in smaller fluctuations for the length d (1.3-fold smaller), the positions $p_1(x)$ and $p_2(x)$ of the front end and rear end (1.3-fold smaller) and the object's center $p_0(x)$ (1.5-fold smaller) than the correlation method
7. The object's diameter d_y resulting from the correlation method shows smaller fluctuations than the diameter resulting from the convolution method (1.1-fold smaller)

Taken together, the results (Fig. 7a) indicate that the precision of either algorithm strongly depends on both the SNR of the images and the size of the object (compare the left and right parts of Fig. 7a). While the convolution algorithm leads to a more precise

estimate for the object length d, the correlation algorithm results instead in a more precise diameter d_y. How can this result be explained? The precision of the correlation algorithm depends on the slope of the correlation function (Walker et al. 1994). For instance, increasing the object length in the x-direction (while the width is kept constant) results in a broader and shallower correlation function in the x-direction. This effect reduces the detection precision of the edges of the underlying object which are perpendicular to this axis. This does not apply, however, to the convolution algorithm. An increase, for example, in the length d_x of the object's middle part (see Fig. 3a) (while all other parameters are kept constant) leaves the intensity distribution at the edges of the object unchanged provided that the diameter of the confocal detection volume (or the point-spread function of the microscope) is small compared to the length d_x; in other words $2r_{xy} < d_x$. In this case, the detection precision of the object's rear and front end $p_1(x)$ and $p_2(x)$ (the positions of the edges perpendicular to the x-axis) should be unchanged, whereas the detection precision of the object's left and right border $p_3(y)$ and $p_4(y)$ (the positions of the edges parallel to the x-axis) should increase. The latter effect is a direct consequence of the increased number of data points that form the borders of the object parallel to the x-axis.

To confirm these statements we analyzed the detection precision of the characteristic object points $p_0(x)$, $p_1(x)$, $p_2(x)$, $p_0(y)$, $p_3(y)$, $p_4(y)$, as well as the length d_x and the width d_y of the object as a function of the length d_x of the underlying object. To allow a direct comparison between the detection precision of the edges along the x- and y-axes, we analyzed simulated images of a simple theoretical dye-filled box of length d_x and width d_y. For each parameter combination we simulated a set of 500 images with a mean SNR of 11 (for parameters used, see legend of Fig. 7) and applied the convolution and correlation algorithm.

The results in Fig. 7c obviously confirm that the detection precision of the object points $p_0(x)$, $p_1(x)$ and $p_2(x)$ with respect to the x-axis resulting from the convolution method does not depend on the length d_x of the underlying object ($d_x > 2r_{xy}$), whereas the precision resulting from the correlation method decreases (σ increases) with increasing length d_x (left part of Fig. 7c). Also, the detection precision of the object points $p_0(y)$, $p_3(y)$ and $p_4(y)$ with respect to the y-axis increases with increasing length d_x for either algorithm (right part of Fig. 7c). As expected, the corresponding bias of the measured parameters is significantly smaller in this case compared to the bias of the simulations above (Fig. 7b versus Fig. 7d) because of the higher number of images simulated for each parameter combination (500 instead of 100). Also, the bias for the measured parameters is within the same range for either algorithm (Fig. 7d).

From the data shown in Fig. 7c (left part) it is apparent that the length d_x resulting from the correlation method shows smaller fluctuations than the length resulting from the convolution method if the length of the object is smaller than $\sim 7.5 r_{xy}$ ($r_{xy} = 2.5$ pixels). For $d_x < 5.5 r_{xy}$ and $d_x < 3.5 r_{xy}$, respectively, this is also true for the object points $p_1(x)$ and $p_2(x)$ and the object's center $p_0(x)$, respectively (Fig. 7c, left part). Taken together, the correlation algorithm results in more precise estimates than the convolution algorithm if the diameter of the object is smaller than about four to five times the waist radius r_{xy}.

This result suggests that when tracking small objects (small fluorescence-labeled vesicles or fluorescent molecules), the two-step correlation algorithm presented here is the method of choice in terms of precision. For example, analyzing a set of 500 simulated images ($r_{xy} = 2.5$ pixels) of a stationary dye-filled box with a length and width of only one pixel (with a typical pixel size of 100 nm this would correspond to the size of a small vesicle), results in 1.5-fold more precise object positions $p_1(x)$, $p_2(x)$, $p_3(y)$, $p_4(y)$, length d_x and width d_y, and in a 1.24-fold more precise object center $p_0(x)$ and $p_0(y)$, respectively.

The most plausible explanation for this outcome is the noise reduction due to the correlation analysis, which has obviously a larger effect in the case of small objects. For larger objects, the reduction in the precision due to the decreased slope of the correlation function dominates as discussed above. In contrast to the common cross-correlation algorithms that use a fixed template (or kernel), each image of a sequence has its own optimized template, and, therefore, the filter effect due to the cross-correlation calculation is optimal. As outlined above, the template's parameters are derived from the ACF analysis. (Alternatively, the template could be determined using the convolution method, the advantage there being speed.) We have shown (Fig. 7b) that accurate object parameters can be obtained from the ACF analysis despite the replacement of the central ACF peak by an appropriate value, as described in the "Theory" section. Ideally, the intensity distributions of the wild-type object and the templates of the object have the same spectra. Therefore, a part of the superimposed noise spectrum is suppressed in an optimal way. Because the theoretical correlation function $G(\xi,\eta)$ (Eq. 33, together with 6 and 7) does not contain any noise (it instead contains the background constant g_B), the fit algorithm results in more precise parameters. An increased object diameter leads, however, to a decreased correlation function slope and thus to a reduced edge detection precision. This effect is contrary to the noise removal performed by correlation analysis.

At this point in our study, the appropriateness of the slice model has been demonstrated, the convolution analysis has been found to give more precise estimates than the correlation method for the front and rear end of the bacteria, and it has been shown that the precision of either algorithm increases with increasing SNR. These results now allow us to analyze image sequences of *E. coli* using the convolution algorithm.

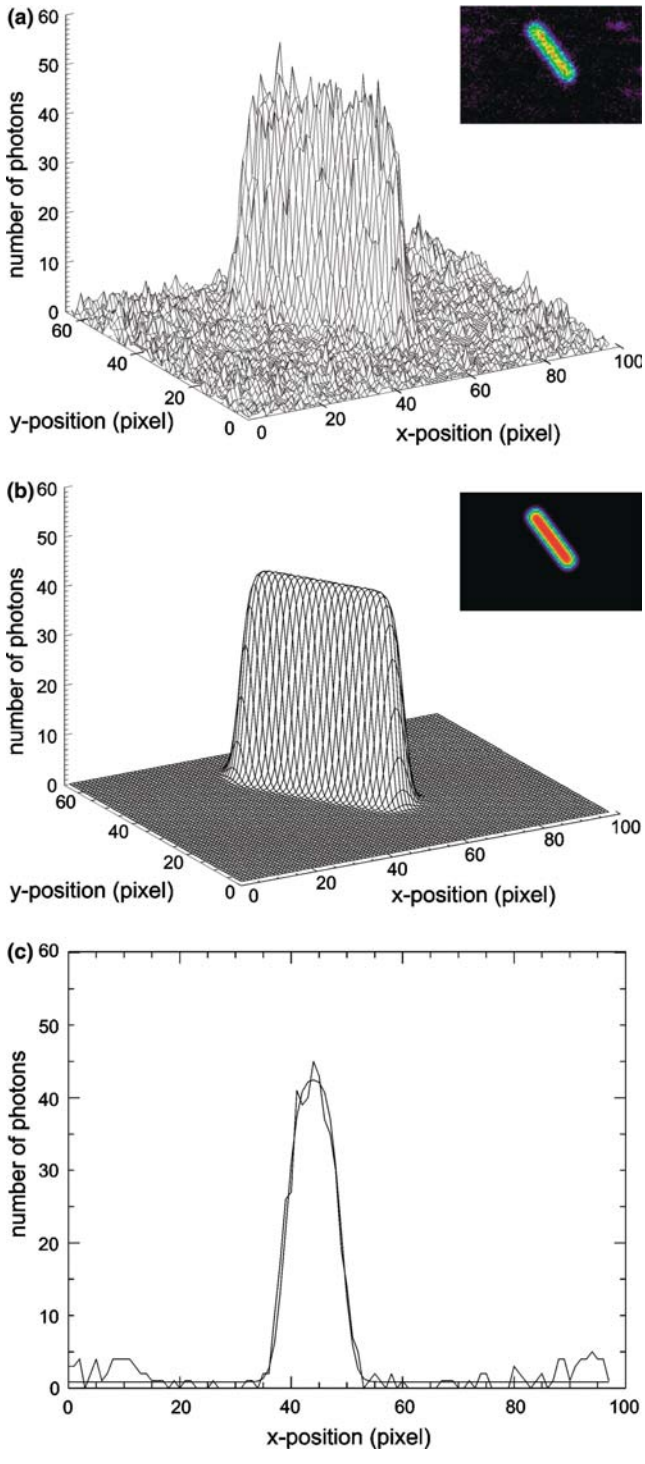

Fig. 8a–c CLSM measurement and convolution analysis of a stationary *E. coli* bacterium stained with MitoTracker Orange. **a** Intensity distribution of the bacterium (first image of a sequence of 100 measured images). Image size: 98×64 pixels; pixel dwell time: 3.45 µs; pixel size: 88 nm. **b** Fitted theoretical intensity distribution $\mathcal{I}_{\mathrm{obj}}(x,y)$ of a slice model (Eq. 11 with Eqs. 6, 7, 38 and 39). Result of the fit: $d_x = 2448.9$ nm, $d_1 = 495.4$ nm ($d_2 = d_1$, fixed), $d_y = 804.5$ nm, $I_B = 0.85308$, $\tilde{x}_0 = 1.525$ pixels; $\tilde{y}_0 = -62.165$ pixels and $\phi = 2.21297$ ($\chi^2 = 13005.65$). These data result in an *E. coli* length of $d = 3439.7$ nm. **c** x-sections through the experimental and fitted intensity distributions at $y = 45$. The mean SNR of the images was 11.21 ± 0.43

Image analysis of stationary *E. coli*

As experimental examples, we took sequences of stationary *E. coli*, with sequences taken at different levels of *E. coli* staining. Figure 8a shows the first image of a sequence of 100 images and (b) shows the intensity $\mathcal{I}_{\mathrm{obj}}(x,y)$ of the slice model fitted to it. A x-section through the experimental and theoretical intensity distribution at $y = 45$ is shown in Fig. 8c. The fitting procedure easily yields values for the five points indicated in the inset of Fig. 9a, namely the center, the front end, the rear end, the right border and the left border of the bacterium, indicated by p_0, p_1, p_2, p_3, p_4. When these values are plotted for the 100 images of a sequence (Fig. 9a, right), the fluctuations of these points can hardly be noticed. In (b) of this figure we therefore plotted the trajectories of the five characteristic points, p_0, p_1, p_2, p_3, p_4, of the bacterium at higher magnification, leaving their relative orientation unchanged (their distances from each other are therefore not to scale). This figure clearly demonstrates (i) that while the center (p_0) exhibits the smallest fluctuations, the front (p_1) and rear end (p_2) exhibit the largest ones, and (ii) that the fluctuations are anisotropic, the fluctuations in the direction of the bacterium's major symmetry axis being markedly larger (Fig. 9c). Table 1 gives the standard deviations of the five points in the $\tilde{x}$ - and $\tilde{y}$ -directions of the coordinate system $\tilde{O}$. Carrying out the analysis using the additional constraint $d_1 = d_2 = d_y/2$, (with the same number of fit parameters for the length and the width of the object) results in slightly smaller standard deviations for the front and rear end ($\sigma_{\tilde{x}}(p_1) = 13.2$ nm and $\sigma_{\tilde{x}}(p_2) = 15.5$ nm), while the values for the other parameters (see Table 1) do not change significantly.

When the same experiment was carried out at a higher level of *E. coli* staining and at a fluorescence emission where the avalanche photodiode saturates, the shape of the image (Fig. 10a) as well as that of the model (Fig. 10b) changes characteristically in that the maxima become approximately flat planes. A y-section through the experimental and theoretical intensity distribution at $x = 37$ is shown in Fig. 10c. An additional reason for the pronounced flat intensity maximum is the larger diameter of the *E. coli* compared to the diameter of the bacterium of the first experiment, shown in Fig. 9a. Plotting the same five points as before (Fig. 11a and b) clearly indicates that the precision at which the points can be determined is higher at higher photon count rates (Table 2).

Although the detection of photons at count rates above 1 Mcps is in the non-linear range of the APD (Fig. 2a, inset), the bias caused by the non-linearity of the APD for detecting relative displacements is small compared to the experimentally-achievable precision. Correcting for the non-linearity, in other words calculating the deadtime-corrected intensity distribution $\mathcal{I}'_{\mathrm{obj}}(x,y)$ (see legend of Fig. 2a) from the fitted intensity distribution shown in Fig. 10b, and re-evaluating the resulting corrected distribution with the intensity distribution $\mathcal{I}_{\mathrm{obj}}(x,y)$ demonstrates that small symmetric

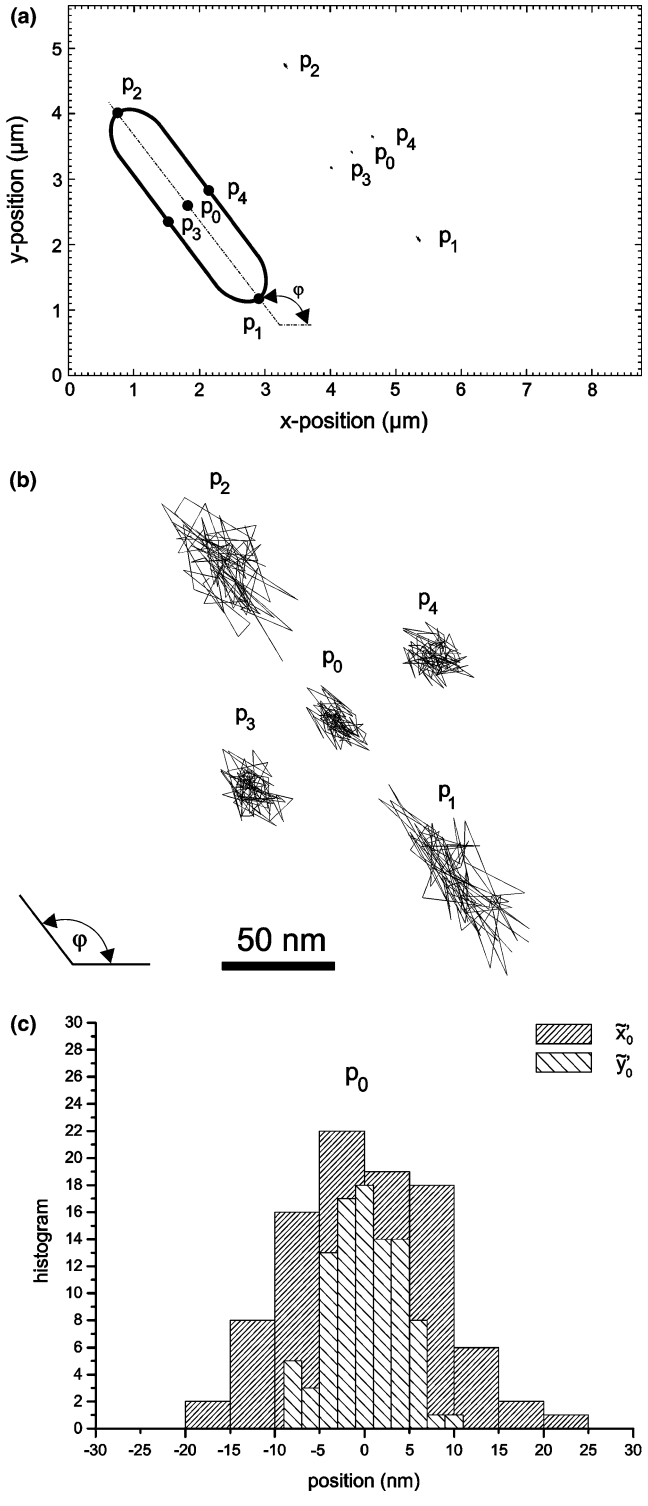

Fig. 9a–c Result of the convolution analysis of an image sequence taken of an immobile *E. coli* bacterium (the first image of the sequence is shown in Fig. 8a).**a** Trajectories of the estimated positions of the characteristic object points p_0, p_1, p_2, p_3 and p_4 (middle part of the figure). A schematic of the model object with the indicated object points is drawn on the left part of the figure. **b** Trajectories of the positions at higher magnification with unchanged relative orientation (the distances between the trajectories of the characteristic points are not to scale). **c** Distributions of the measured distances, $\tilde{x}'_0 = \tilde{x}_0 - \langle\tilde{x}_0\rangle$ and $\tilde{y}'_0 = \tilde{y}_0 - \langle\tilde{y}_0\rangle$, from the mean localized object center $\langle p_0\rangle = (\langle\tilde{x}_0\rangle, \langle\tilde{y}_0\rangle)$ with respect to the $\tilde{x}$ - and $\tilde{y}$ -axes of the rotated coordinate system $\tilde{O}$

Table 1 Standard deviations $\sigma_{\tilde{x}}$ and $\sigma_{\tilde{y}}$ of the localized object points p_0 to p_4 shown in Fig. 9a and b

Object point	p_0	p_1	p_2	p_3	p_4
$\sigma_{\tilde{x}}$ (nm)	8.4	21.6	18	8.9	8.1
$\sigma_{\tilde{y}}$ (nm)	4.3	7.3	9.2	6.1	6.2

and asymmetric length changes can still be detected precisely. This can be illustrated as follows: let us first increase the length of the model object by $\Delta d = \Delta d_x = 0.1$ pixels (all other parameters kept unchanged; for parameters used, see legend of Fig. 10), then re-calculate both the corresponding theoretical distribution $\mathcal{I}_{\text{obj}}(x,y)$ and its deadtime-corrected intensity distribution $\mathcal{I}'_{\text{obj}}(x,y)$, and finally fit the former and the resulting deadtime-corrected intensity distribution using the distribution $\mathcal{I}_{\text{obj}}(x,y)$ of the slice model. This results in a detected length increase for the object of $\Delta d = 0.093$ pixels. For a pixel size of 88 nm, this deviation corresponds to a few Angstroms and is thus not significant here.

As pointed out in the "Methods" section, the deadtime of the APD results in an increased relative standard deviation of the photodetector count rate and therefore in a reduced SNR of the experimental images. Furthermore, small thermal fluctuations of the *E. coli* membrane and small movements of the bacterium itself might have contributed to the measured precision. The measured standard deviations for the object points (Table 1 and 2) thus reflect the upper limits for the precision that can be achieved. Taken together, these results clearly demonstrate that the position and size parameters of objects such as bacteria can be determined well below the resolution limit of the objective.

Conclusions and perspective

In this paper we have provided algorithms that allow the tracking of finite microscopical regularly shaped objects, determining their position, orientation and size parameters. Whereas the tracking of point sources has been dealt with in detail (see, for example, Saxton and Jacobson 1997), simultaneous measurement of position, shape and size parameters of finite living particles at the nanometer scale has as yet not been reported. In order to demonstrate the precision of the algorithms we restricted our study to stationary objects, but the algorithms can, without any change, be applied to moving particles. However, caution is necessary when applying the algorithms to images of objects with a component of movement along the optical axis, as a vertically-tilted object would appear shorter than it actually is. Hence,

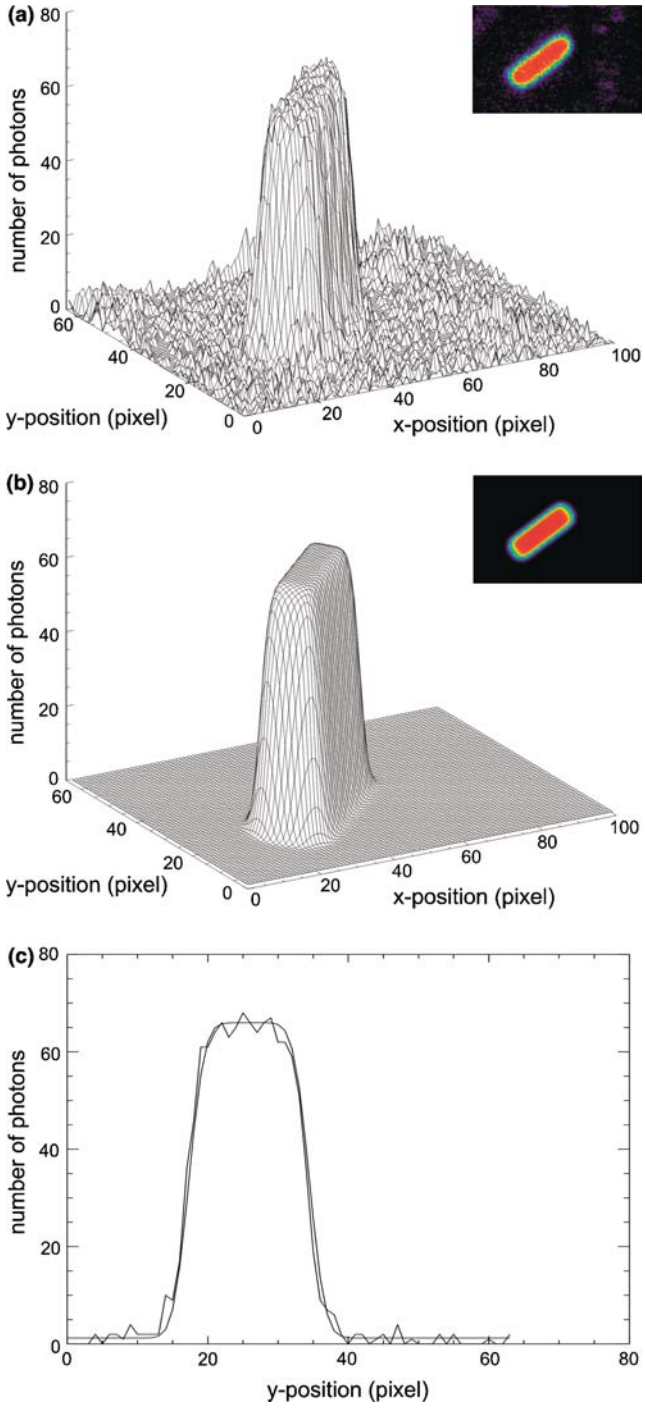

Fig. 10a–c CLSM measurement and convolution analysis of an immobile *E. coli* bacterium stained with MitoTracker Orange.**a** Intensity distribution of the bacterium (first image of a sequence of 120 measured images). Image size: 100×64 pixels; pixel dwell time: 3.4 µs; pixel size: 88 nm. **b** Fitted theoretical intensity distribution $\mathcal{I}_{\mathrm{obj}}(x,y)$ of a slice model (Eq. 11 with Eqs. 6, 7, 38 and 39). Result of the fit: $d_x = 2294.3$ nm, $d_1 = 826.7$ nm ($d_2 = d_1$, fixed), $d_y = 1363.2$ nm, $I_B = 0.7036$, $\tilde{x}_0 = 49.811$ pixels; $\tilde{y}_0 = 0.1377$ pixels and $\phi = 0.647$ ($\chi^2 = 20138.71$). These data result in an *E. coli* length of $d = 3947.8$ nm. **c** *y*-section through the experimental and fitted intensity distribution at $x = 37$. The mean SNR of the images was 16.34 ± 0.37

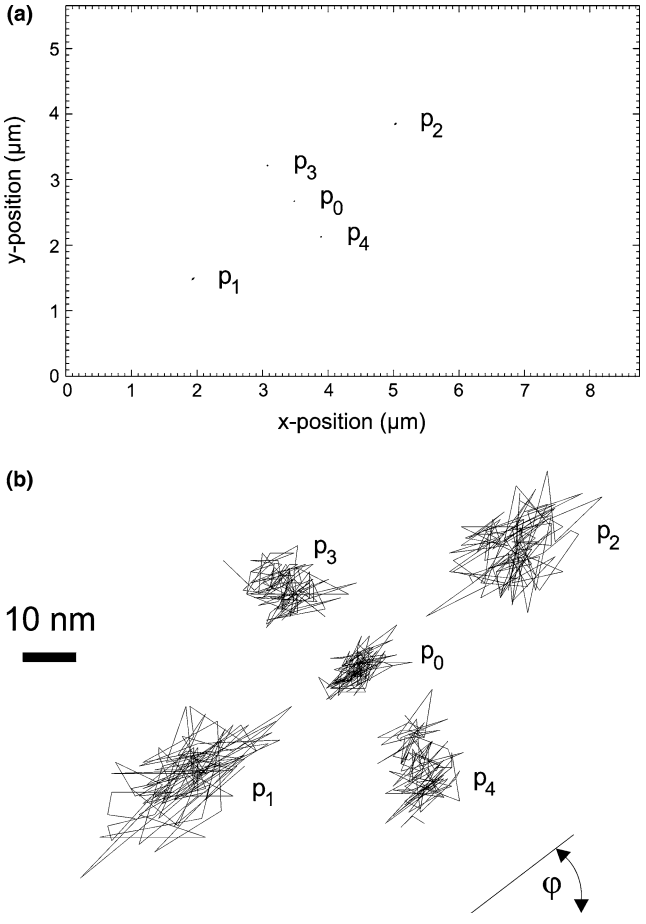

Fig. 11a–b Results from the convolution analysis of an image sequence taken of a stationary *E. coli* bacterium at high fluorescence emission (the first image of the image sequence is shown in Fig. 10a). **a** Trajectories of the estimated positions of the object points p_0, p_1, p_2, p_3, p_4. **b** Higher magnification with unchanged relative orientation (distances between the characteristic points not to scale)

Table 2 Standard deviations $\sigma_{\tilde{x}}$ and $\sigma_{\tilde{y}}$ of the localized object points p_0 to p_4 shown in Fig. 11

Object point	p_0	p_1	p_2	p_3	p_4
$\sigma_{\tilde{x}}$ (nm)	3.7	8.7	6.7	3.7	4.1
$\sigma_{\tilde{y}}$ (nm)	1.9	4.1	4.5	3.8	4.6

biological processes that can easily be investigated would be, for instance, the axonal or dendritic transport of vesicles or mitochondria along microtubules oriented parallel to the cover slip. Researchers in this field might find our algorithms particularly useful because they allow, for the first time, the study of sub-microscopic movement-related changes of size and shape of the objects under investigation. The feasibility of such measurements, however, will depend on the velocity of the underlying process. For a given process, a sufficiently small image aquisition time will be necessary to prevent apparent size changes in the object due to motion blur.

The algorithms were quantitatively compared to each other using computer simulations. The correlation algorithm is based on both the autocorrelation analysis of an image and the cross-correlation analysis of an image and its individually-optimized template (calculated from its ACF). Taking into account the entire two-dimensional distribution of the correlation functions, the correlation algorithm results in more precise parameters than the convolution algorithm if the object to be tracked has a diameter smaller than about four to five times the waist radius r_{xy}, whereas the convolution algorithm is more precise if the size of the object exceeds this value. The choice of the appropriate algorithm is therefore a question of the object's size. As the convolution algorithm incorporates the frequently-used Gaussian fit algorithm (Anderson et al. 1992; Schütz et al. 1997; Yildiz et al. 2003), it can further be pointed out that the correlation algorithm introduced is also superior to the Gaussian fit algorithm, leading to more precise estimates in cases where single fluorescent molecules are to be tracked. This is not necessarily true, however, for other correlation algorithms (Cheezum et al. 2001), that take into account only the peaks of the two-dimensional cross-correlation functions.

The precision by which the object's size and position parameters can be determined is remarkable. At high intensity signals, the precision can be driven to the lower nanometer range. The quality of the fit of the above delineated models to the experimental data depends on the number of photons gathered and the signal-to-noise ratio. With respect to the photon detection efficiency and the negligible dark-count rate, the APD is an ideal sensor at low count rates. However, as we demonstrated with our experiments, the smaller dynamic range of the APD becomes limiting at count rates above 1 MHz. To avoid deadtime corrections and to further increase the signal-to-noise ratio of the images and thus the precision of the measurements, the use of a low-noise PMT or back-illuminated CCD-camera (in combination with wide-field microscopy) is recommended when measuring predominantly high intensity signals.

We have compared the sausage model and the slice model in detail and demonstrated that the slice model is an excellent approximation of a sausage-like object, such as an *E. coli* bacterium, if the geometrical parameters of the slices are properly chosen. As Cheezum et al. (2001) pointed out, there is usually no a priori information concerning the precise shape of the object to be measured. Imperfections in the shape could potentially lead to unprecise measurements. Generally, the best fitting geometrical model has to be adopted. Further, inhomogeneous staining of the object under investigation (especially at the object boundaries) could bias the measurement. It will therefore be necessary to optimize the labeling technique (using exogenous dyes or fluorescent genetic markers) to achieve sufficient homogeneous object staining and to find out the most appropriate model for every object under investigation. However, the sausage model can be applied to a number of regularly-shaped organelles. Choosing a model consisting of a stack of slices thus has two advantages. First, it is useful for different object shapes. Second, processor time is markedly reduced due to the separation of integration variables.

Beyond providing algorithms for the measurement and tracking of finite microscopical objects, we show that a precision in the low nanometer range can be achieved in vitro from the properties of the optical configuration of our set-up. The achievable tracking precision for in vivo measurements, however, will depend mainly on the labeling technique (fluorescence yield of the organelle under investigation versus background fluorescence from the surrounding cytoplasm and the cytoskeleton), the distance between labeled organelles, and the quality of the photon detection system. We reason that, when using both an optimized microscopy set-up and fluorescent genetic markers, signal-to-noise ratios between 5 and 20 and even beyond will be achievable. Thus a tracking precision down to a few nanometers could be achievable when studying, say, organelle transport in axons and dendrites of cultured neurons. Using our finite-particle tracking (FPT) algorithms, for instance in the motor protein field, will presumably allow the measurement of movement-related size changes of intracellular cargoes such as mitochondria or vesicles.

Appendix A

Derivation of Eq. 10 leads to the three intensity contributions of the first cap, the shaft, and the second cap of the model bacterium: $I_{\mathrm{obj}}^{\mathrm{ell1}}(\tilde{x},\tilde{y})$, $I_{\mathrm{obj}}^{\mathrm{cyl}}(\tilde{x},\tilde{y})$ and $I_{\mathrm{obj}}^{\mathrm{ell2}}(\tilde{x},\tilde{y})$, respectively,

$$
\begin{aligned}
I_{\mathrm{obj}}^{\mathrm{ell1}}(\tilde{x},\tilde{y}) = q \int_{-d_1}^{0} \mathrm{d}x' \int_{0}^{1} \mathrm{d}\eta \int_{0}^{2\pi} \mathrm{d}\theta\, \eta \left(\frac{d_y}{2}\right)^2 \left(1-\frac{x'^2}{d_1^2}\right) \\
\times \exp\left[-2(\tilde{x}-\tilde{x}_0+d_x/2-x')^2 \Big/ r_{xy}^2\right] \\
\times \exp\Big[-2\{\tilde{y}-\tilde{y}_0-(d_y/2) \\
\times \left(1-x'^2/d_1^2\right)^{1/2} \eta\cos\theta\}^2 \Big/ r_{xy}^2\Big] \\
\times \exp\left[-2\left(d_y/2\right)^2\left(1-x'^2/d_1^2\right)\eta^2\sin^2\theta/r_z^2\right],
\end{aligned}
\tag{34}
$$

$$
\begin{aligned}
I_{\mathrm{obj}}^{\mathrm{cyl}}(\tilde{x},\tilde{y}) = q \int_{-d_x/2}^{d_x/2} \mathrm{d}x' \int_{0}^{d_y/2} \mathrm{d}r \int_{0}^{2\pi} \mathrm{d}\theta \cdot r \\
\times \exp\left[-2(\tilde{x}-\tilde{x}_0-x')^2 \Big/ r_{xy}^2\right] \\
\times \exp\left[-2(\tilde{y}-\tilde{y}_0-r\cos\theta)^2 \Big/ r_{xy}^2\right] \\
\times \exp\left[-2r^2\sin^2\theta/r_z^2\right],
\end{aligned}
\tag{35}
$$

and

$$I_{\mathrm{obj}}^{\mathrm{ell2}}(\tilde{x},\tilde{y}) = q\int_0^{d_2}\mathrm{d}x'\int_0^1\mathrm{d}\eta\int_0^{2\pi}\mathrm{d}\theta\,\eta\left(\frac{d_y}{2}\right)^2\left(1-\frac{x'^2}{d_2^2}\right)$$
$$\times\exp\left[-2(\tilde{x}-\tilde{x}_0-d_x/2-x')^2\Big/r_{xy}^2\right]$$
$$\times\exp\left[-2\left\{\tilde{y}-\tilde{y}_0-\left(d_y\Big/2\right)\right.\right.$$
$$\left.\left.\times\left(1-x'^2/d_2^2\right)^{1/2}\eta\cos\theta\right\}^2\Big/r_{xy}^2\right]$$
$$\times\exp\left[-2\left(d_y/2\right)^2\left(1-x'^2/d_2^2\right)\eta^2\sin^2\theta/r_z^2\right], \tag{36}$$

where

$$q = \langle C\rangle gQI_{\mathrm{a}}. \tag{37}$$

Appendix B

Carrying out the numerical optimization procedure for the hemiellipsoidal caps leads to the following parameters for the slices:

$$\begin{aligned} x_{\mathrm{A}} &= 0.305579\times d_1\\ x_{\mathrm{B}} &= 0.585352\times d_1\\ x_{\mathrm{D}} &= 0.585352\times d_2\\ x_{\mathrm{E}} &= 0.305579\times d_2\\ y_{\mathrm{A}} &= y_{\mathrm{E}} = 0.593244\times d_y\\ y_{\mathrm{B}} &= y_{\mathrm{D}} = 0.843075\times d_y, \end{aligned} \tag{38}$$

whereas the width

$$y_{\mathrm{C}} = \sqrt{\pi}d_y/2 \tag{39}$$

of the middle slice of length $x_C = d_x$ (see Fig. 3b) follows directly from the requirement that the cylinder and slice volume be identical, in other words $\pi\, d_y^2 d_x/4 = y_C^2 d_x$.

Appendix C

The five intensity distributions describing the the slice model (Eq. 11), are given by

$$\mathcal{I}_{\mathrm{A}}(\tilde{x},\tilde{y}) = p\times\mathrm{erf}\left(\frac{z_{\mathrm{A}}}{\sqrt{2}r_z}\right)$$
$$\times\left\{\mathrm{erf}\left(\frac{\sqrt{2}}{r_{xy}}\left[\tilde{x}-\tilde{x}_0+\frac{x_{\mathrm{C}}}{2}+x_{\mathrm{B}}+x_{\mathrm{A}}\right]\right)\right.$$
$$\left.-\mathrm{erf}\left(\frac{\sqrt{2}}{r_{xy}}\left[\tilde{x}-\tilde{x}_0+\frac{x_{\mathrm{C}}}{2}+x_{\mathrm{B}}\right]\right)\right\}$$
$$\times\left\{\mathrm{erf}\left(\frac{\sqrt{2}}{r_{xy}}\left[\tilde{y}-\tilde{y}_0+\frac{y_{\mathrm{A}}}{2}\right]\right)\right.$$
$$\left.-\mathrm{erf}\left(\frac{\sqrt{2}}{r_{xy}}\left[\tilde{y}-\tilde{y}_0-\frac{y_{\mathrm{A}}}{2}\right]\right)\right\}, \tag{40}$$

$$\mathcal{I}_{\mathrm{B}}(\tilde{x},\tilde{y}) = p\times\mathrm{erf}\left(\frac{z_{\mathrm{B}}}{\sqrt{2}r_z}\right)$$
$$\times\left\{\mathrm{erf}\left(\frac{\sqrt{2}}{r_{xy}}\left[\tilde{x}-\tilde{x}_0+\frac{x_{\mathrm{C}}}{2}+x_{\mathrm{B}}\right]\right)\right.$$
$$\left.-\mathrm{erf}\left(\frac{\sqrt{2}}{r_{xy}}\left[\tilde{x}-\tilde{x}_0+\frac{x_{\mathrm{C}}}{2}\right]\right)\right\}$$
$$\times\left\{\mathrm{erf}\left(\frac{\sqrt{2}}{r_{xy}}\left[\tilde{y}-\tilde{y}_0+\frac{y_{\mathrm{B}}}{2}\right]\right)\right.$$
$$\left.-\mathrm{erf}\left(\frac{\sqrt{2}}{r_{xy}}\left[\tilde{y}-\tilde{y}_0-\frac{y_{\mathrm{B}}}{2}\right]\right)\right\}, \tag{41}$$

$$\mathcal{I}_{\mathrm{C}}(\tilde{x},\tilde{y}) = p\times\mathrm{erf}\left(\frac{z_{\mathrm{C}}}{\sqrt{2}r_z}\right)\left\{\mathrm{erf}\left(\frac{\sqrt{2}}{r_{xy}}\left[\tilde{x}-\tilde{x}_0+\frac{x_{\mathrm{C}}}{2}\right]\right)\right.$$
$$\left.-\mathrm{erf}\left(\frac{\sqrt{2}}{r_{xy}}\left[\tilde{x}-\tilde{x}_0-\frac{x_{\mathrm{C}}}{2}\right]\right)\right\}$$
$$\times\left\{\mathrm{erf}\left(\frac{\sqrt{2}}{r_{xy}}\left[\tilde{y}-\tilde{y}_0+\frac{y_{\mathrm{C}}}{2}\right]\right)\right.$$
$$\left.-\mathrm{erf}\left(\frac{\sqrt{2}}{r_{xy}}\left[\tilde{y}-\tilde{y}_0-\frac{y_{\mathrm{C}}}{2}\right]\right)\right\}, \tag{42}$$

$$\mathcal{I}_{\mathrm{D}}(\tilde{x},\tilde{y}) = p\times\mathrm{erf}\left(\frac{z_{\mathrm{D}}}{\sqrt{2}r_z}\right)\left\{\mathrm{erf}\left(\frac{\sqrt{2}}{r_{xy}}\left[\tilde{x}-\tilde{x}_0-\frac{x_{\mathrm{C}}}{2}\right]\right)\right.$$
$$\left.-\mathrm{erf}\left(\frac{\sqrt{2}}{r_{xy}}\left[\tilde{x}-\tilde{x}_0-\frac{x_{\mathrm{C}}}{2}-x_{\mathrm{D}}\right]\right)\right\}$$
$$\times\left\{\mathrm{erf}\left(\frac{\sqrt{2}}{r_{xy}}\left[\tilde{y}-\tilde{y}_0+\frac{y_{\mathrm{D}}}{2}\right]\right)\right.$$
$$\left.-\mathrm{erf}\left(\frac{\sqrt{2}}{r_{xy}}\left[\tilde{y}-\tilde{y}_0-\frac{y_{\mathrm{D}}}{2}\right]\right)\right\}, \tag{43}$$

and

$$\mathcal{I}_{\mathrm{E}}(\tilde{x},\tilde{y}) = p \times \mathrm{erf}\left(\frac{z_E}{\sqrt{2}r_z}\right)\left\{\mathrm{erf}\left(\frac{\sqrt{2}}{r_{xy}}\left[\tilde{x}-\tilde{x}_0-\frac{x_{\mathrm{C}}}{2}-x_{\mathrm{D}}\right]\right)\right.$$
$$\left.-\mathrm{erf}\left(\frac{\sqrt{2}}{r_{xy}}\left[\tilde{x}-\tilde{x}_0-\frac{x_{\mathrm{C}}}{2}-x_{\mathrm{D}}-x_{\mathrm{E}}\right]\right)\right\}$$
$$\times\left\{\mathrm{erf}\left(\frac{\sqrt{2}}{r_{xy}}\left[\tilde{y}-\tilde{y}_0+\frac{y_{\mathrm{E}}}{2}\right]\right)\right.$$
$$\left.-\mathrm{erf}\left(\frac{\sqrt{2}}{r_{xy}}\left[\tilde{y}-\tilde{y}_0-\frac{y_{\mathrm{E}}}{2}\right]\right)\right\}, \tag{44}$$

where

$$p = \langle C\rangle g Q I_{\mathrm{a}} \frac{1}{4}\left(\frac{\pi}{2}\right)^{3/2} r_{xy}^2 r_z. \tag{45}$$

Appendix D

The slice model can only be preferred if the error introduced by approximating the sausage model by slices is acceptable. The question to be answered here is therefore: how well does the slice model approximate the sausage model?

Let us adopt the sausage model assuming morphologically-realistic *E.coli* parameters, and then calculate the resulting fluorescence intensity $I_{\mathrm{obj}}(x,y)$ according to Eq. 10 (Fig. 12a). A cross-section at $y=32$ through its maximum is shown by the continuous curves shown in (b) and (c) of this figure. Then we fit the intensity distribution $\mathcal{I}_{\mathrm{obj}}(x,y)$ (Eq. 11 with Eqs.38 and 39) of the corresponding slice model to the calculated intensity distribution of the sausage model. A section through this function at $y=32$ gives the dashed curve shown in Fig. 12b. Though the maximum amplitude of the sausage object is underestimated by the slice model fit, the front and rear edge of the intensity distribution are almost perfectly fitted (Fig. 12b, dashed versus continuous curve) due to the good approximation of the bacterium's caps by the stack of slices (Fig. 3c). As the front and rear edge of the intensity distribution are well described by the intensity distribution of the slice model, the resulting length parameter of $d=36.018$ pixels is in good agreement with the length

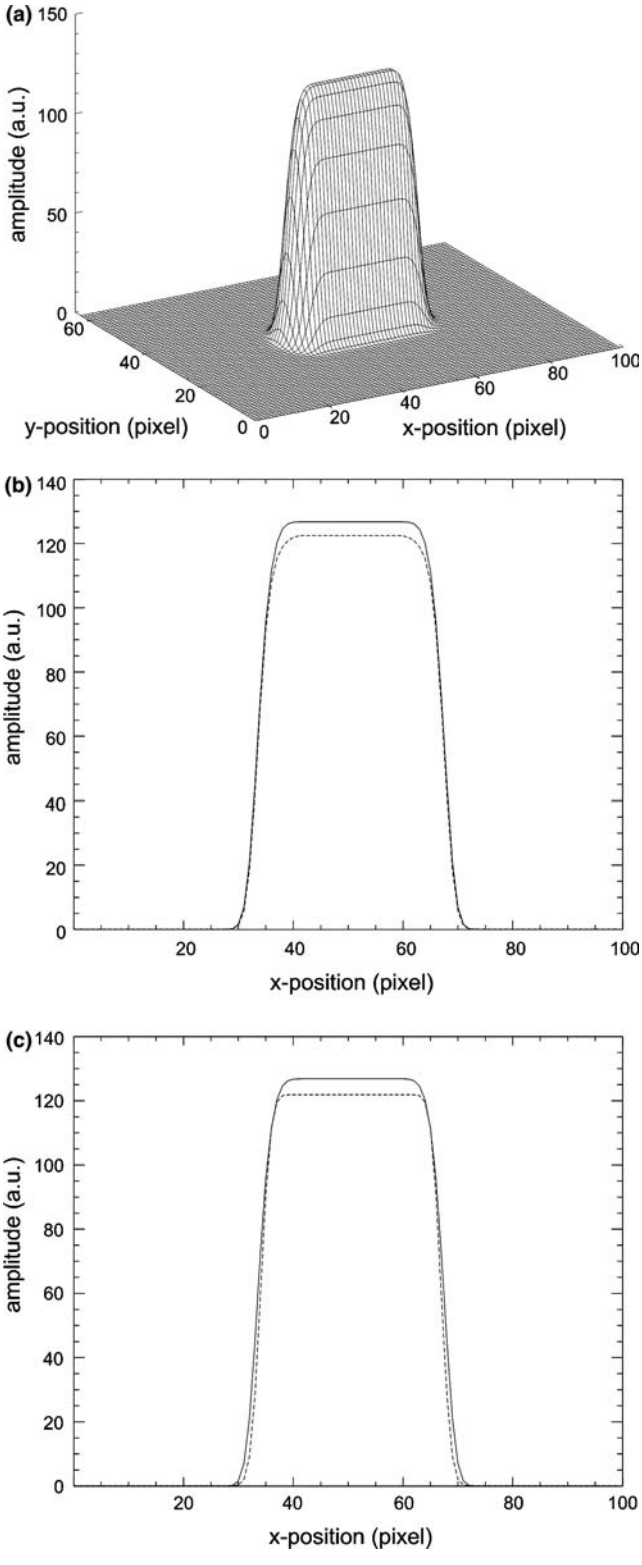

Fig. 12a–c Intensity distribution of the sausage model and its approximation by the intensity distributions of a slice and a box model, respectively.**a** Theoretical distribution $I_{\mathrm{obj}}(x,y)$ (Eq. 10, $x=\tilde{x}$ and $y=\tilde{y}$) of the sausage model, calculated with the parameters: $d_x=25$ pixels, $d_1=d_2=5.5$ pixels, $d_y=11$ pixels, $\phi=0$ and $p_0=(49,32)$. *E. coli* length: $d=36$ pixels. **b** *x*-section through the intensity distribution of the sausage model shown in (a) (*solid line*) and through the fitted intensity distribution $\mathcal{I}_{\mathrm{obj}}(x,y)$ (Eq. 11 with Eqs. 6, 7, 38 and 39) of the slice model (*dashed line*) both at $y=32$. Result of the fit: $d_x=24.7$ pixels, $d_1=5.66$ pixels, $d_2=5.658$ pixels, $d_y=10.492$, $x_0=49$ pixels, $y_0=32$ pixels and $\phi=0$ ($\chi^2=5456.97$). These data result in an object length of $d=36.018$ pixels.**c** Fitting the intensity distribution of a simple box model (Eq. 11 with $d_1=d_2=0$) gave (*dashed line*): $d_x=32.886$ pixels, $d_y=10.3$ pixels and $\phi=0$ ($\chi^2=15250.22$)

of $d = 36$ pixels of the underlying sausage model. For a given pixel size of 88 nm, this corresponds to a deviation of 1.6 nm, much smaller than the experimental precision that can be achieved under our conditions (see below).

The negligible error of the slice model approximation suggests that a simple box model (a slice model with just one slice) might be sufficient to approximate the sausage model. However, assuming a slice model with $d_1 = d_2 = 0$ (just one box without the hemiellipsoidal caps attached to it, Fig. 3), a clear deviation between the distributions is seen at the edges (Fig. 12c). A box model is thus too coarse for assessing the bacterium's edges. This is also reflected in the larger deviation between the resulting width of $d_y = 10.492$ of the box model and the exact width of $d_y = 11$ pixels of the sausage model. For the same pixel size, this would correspond to a bias of $\sim$51 nm. The reason for this discrepancy is obviously the mismatch between the rectangular cross-sections of the slice model and the circular cross-sections of the sausage model. If the slice model is used instead for determining the relative displacements of the left and right borders of the sausage model, the bias becomes much smaller: increasing the width d_y of the sausage model from 11 pixels to 11.1 pixels (all other parameters kept unchanged, see legend of Fig. 12), and analyzing the resulting intensity distribution $I_{\mathrm{obj}}(x,y)$ with the distribution $\mathcal{I}_{\mathrm{obj}}(x,y)$ of the slice model, results in a width of $d_y = 10.59$ pixels. The detected increase of the width of the object of $\Delta d_y = 0.098$ pixels is in excellent agreement with the exact change of 0.1 pixels. For a pixel size of 88 nm, the deviation would therefore be a few Angstroms. Another convenient feature of the slice model is that small length changes of a non-symmetric sausage model ($d_1 \neq d_2$) can be detected using a symmetric slice model ($d_1 = d_2$, fixed). This feature allows us to reduce the number of fit parameters. For example, increasing the length of the left hemiellipsoidal cap of the sausage model from $d_1 = 5.5$ pixels to $d_1 = 6$ pixels ($\Delta d_1 = \Delta d = 0.5$) while the other parameters stay constant, and analyzing the corresponding intensity distribution with the distribution of a symmetric slice model leads to a detected length change of $\Delta d = 0.503$. For 88 nm pixel size, the bias is therefore again a few Angstroms.

Taken together, these results show that the slice model gives reliable results when used to determine the absolute length of sausage-like objects such as *E. coli* bacteria, or when used to detect relative length and width changes.

References

Anderson CM, Georgiou GN, Morrison IEG, Stevenson GVW, Cherry RJ (1992) Tracking of cell surface receptors by fluorescence digital imaging microscopy using a charged-coupled device camera. J Cell Sci 101:415-425

Bobroff N (1986) Position measurement with a resolution and noise-limited instrument. Rev Sci Instrum 57:1152-1157

Cheezum MK, Walker WF, Guilford WH (2001) Quantitative comparison of algorithms for tracking single fluorescent particles. Biophys J 81:2378-2388

Gennerich A, Schild D (2000) Fluorescence correlation spectroscopy in small cytosolic compartments depends critically on the diffusion model used. Biophys J 79:3294-3306

Gennerich A, Schild D (2002) Anisotropic diffusion in mitral cell dendrites revealed by fluorescence correlation spectroscopy. Biophys J 83:510-522

Kim SA, Schwille P (2003) Intracellular applications of fluorescence correlation spectroscopy: prospects for neuroscience. Curr Opin Neurobiol 13:583-590

Krichevsky O, Bonnet G (2002) Fluorescence correlation spectroscopy: the technique and its application. Rep Prog Phys 65:251-297

Kues T, Peters P, Kubitscheck U (2001) Visualization and tracking of single protein molecules in the cell nucleus. Biophys J 80:2954-2967

Marquarth DW (1963) An algorithm for least-squares estimation of nonlinear parameters. J Soc Indust Appl Math 11:431-441

Petersen NO, Höddelius PL, Wiseman PW, Seger O, Magnusson KE (1993) Quantitation of membrane receptor distributions by image correlation spectroscopy: concept and application. Biophys J 65:1135-1146

Rigler R, Mets Ü, Widengren J, Kask P (1993) Fluorescence correlation spectroscopy with high count rate and low background: analysis of translational diffusion. Eur Biophys J 22:169-175

Saxton MJ, Jacobson K (1997) Single-particle tracking: applications to membrane dynamics. Annu Rev Biophys Biomol Struct 26:373-399

Schütz GJ, Schindler H, Schmidt T (1997) Single-molecule microscopy on model membranes reveals anomalous diffusion. Biophys J 73:1073-1080

Thompson RE, Larson SR, Webb WW (2002) Precise nanometer localization analysis for individual fluorescent probes. Biophys J 82:2775-2783

Walker WF, Trahey GE (1994) A fundamental limit on the performance of correlation based phase correction and flow estimation techiques. IEEE T Ultrason Ferroelec Freq Cont 41:644-654

Yildiz A, Forkey JN, McKinney SA, Ha T, Goldman YE, Selvin PR (2003) Myosin V walks hand-over-hand: single fluorophore imaging with 1.5-nm localization. Science 300:2061-2065

Yu DF, Fessler JA (2000) Mean and variance of single photon counting with deadtime. Phys Med Biol 45:2043-2056